ORIGINAL ARTICLE

Knock-Down of Hippocampal DISC1 in Immune-Challenged Mice Impairs the Prefrontal–Hippocampal Coupling and the Cognitive Performance Throughout Development

Xiaxia Xu, Lingzhen Song and Ileana L. Hanganu-Opatz

Institute of Developmental Neurophysiology, Center for Molecular Neurobiology, University Medical Center Hamburg-Eppendorf, 20251 Hamburg, Germany

Address correspondence to Ileana L. Hanganu-Opatz, Institute of Developmental Neurophysiology, Center for Molecular Neurobiology, University Medical Center Hamburg-Eppendorf, Falkenried 94, 20251 Hamburg, Germany. Email: hangop@zmnh.uni-hamburg.de or Xiaxia Xu, Institute of Developmental Neurophysiology, Center for Molecular Neurobiology, University Medical Center Hamburg-Eppendorf, Falkenried 94, 20251 Hamburg, Germany. Email: xiaxia.xu@zmnh.uni-hamburg.de.

Xiaxia Xu and Lingzhen Song have contributed equally to this work

Abstract

Disrupted-in-schizophrenia 1 (DISC1) gene represents an intracellular hub of developmental processes. When combined with early environmental stressors, such as maternal immune activation, but not in the absence of thereof, whole-brain DISC1 knock-down leads to memory and executive deficits as result of impaired prefrontal–hippocampal communication throughout development. While synaptic dysfunction in neonatal prefrontal cortex (PFC) has been recently identified as one source of abnormal long-range coupling, the contribution of hippocampus (HP) is still unknown. Here, we aim to fill this knowledge gap by combining in vivo electrophysiology and optogenetics with morphological and behavioral assessment of immune-challenged mice with DISC1 knock-down either in the whole brain (GE) or restricted to pyramidal neurons in hippocampal CA1 area ($G_{HP}E$). We found abnormal network activity, sharp-waves, and neuronal firing in CA1 that complement the deficits in upper layer of PFC. Moreover, optogenetic activating CA1 pyramidal neurons fails to activate the prefrontal local circuits. These deficits that persist till prejuvenile age relate to dendrite sparsification and loss of spines of CA1 pyramidal neurons. As a long-term consequence, DISC1 knock-down in HP leads to poorer recognition memory at prejuvenile age. Thus, DISC1-controlled developmental processes in HP in immune-challenged mice are critical for circuit function and cognitive behavior.

Key words: development, DISC1, hippocampal maturation, optogenetics, prefrontal–hippocampal synchrony

Introduction

Highly dynamic processes control the wiring of neural circuits during development. At its end, reliable communication between brain areas accounts for the complex behavioral abilities of an adult. For example, the coactivation of prefrontal and hippocampal networks in theta–gamma oscillatory rhythms is critical for the precise information flow in mnemonic and executive tasks (Siapas et al. 2005; Spellman et al. 2015; Backus et al. 2016; Eichenbaum 2017). This prefrontal–hippocampal coupling emerges early in life, and the unidirectional drive from the CA1 pyramidal neurons boosts the initial entrainment of local circuits across prefrontal layers (Brockmann et al. 2011; Bitzenhofer et al. 2017b; Ahlbeck et al. 2018). The long-range coupling during development has been proposed to critically contribute to the adult function and cognitive abilities. On the flip side, disease-related dysfunction and poor behavioral performance might result from developmental miswiring (Chini et al. 2020).

The maturation of connectivity and functional coupling within the brain is controlled by numerous cell autonomous processes as well as extracellular and environmental factors. Disrupted-in-schizophrenia 1 (DISC1) is an intracellular scaffold protein that has been identified as an intracellular hub of developmental processes, in particular synapse regulation (Narayan et al. 2013). Despite its name, DISC1 is unlikely to be a "genetic" factor causing schizophrenia (Sullivan et al. 2012; Ripke et al. 2013). Instead, DISC1 has been proven to illustrate the relevance of abnormal development for multiple mental conditions, because it orchestrates molecular cascades hypothesized to underlie disease-relevant physiological and behavioral deficits (Cuthbert and Insel 2013). Mouse models mimicking DISC1 dysfunction have impaired memory and attention as results of disrupted prefrontal–hippocampal circuits (Koike et al. 2006; Niwa et al. 2010; Kvajo et al. 2011; Saito et al. 2016; Crabtree et al. 2017). These deficits are more prominent when environmental stressors, such as maternal immune activation (MIA) additionally disrupt the Disc1 locus (Cash-Padgett et al. 2013a; Lipina et al. 2013). This might be due to the fact that mutated DISC1 modulates the basal or MIA-induced cytokine production by interfering with glycogen synthase kinase-3 (Beurel et al. 2010).

Since DISC1 controls the developmental molecular cascades, it is likely that its dysfunction decisively contributes to early miswiring. Indeed, recent findings revealed that abnormal DISC1 expression perturbs the maturation of prefrontal–hippocampal coupling (Hartung et al. 2016; Oberlander et al. 2019; Xu et al. 2019; Chini et al. 2020). Immune challenged mice with a whole-brain truncated form of DISC1 (dual-hit GE mice) have disorganized oscillatory activity as well as weaker coupling and directed interactions between prefrontal cortex (PFC) and hippocampus (HP) at neonatal age. In contrast, the activity patterns and communication within prefrontal–hippocampal networks as well as the early cognitive abilities were largely unaffected in single-hit genetic (G) (only DISC1 knock-down) or environmental (E) (only MIA) mouse models (Hartung et al. 2016; Oberlander et al. 2019).

The early dysfunction of dual-hit GE mice might result from abnormal activity in either one or both brain areas or from disrupted projections from HP to PFC. Recently, we identified transient neonatal synaptic deficits of prefrontal layer 2/3 pyramidal neurons as one mechanism underlying the abnormal prefrontal–hippocampal communication throughout development (Xu et al. 2019; Chini et al. 2020). However, it is

unknown whether developmental dysfunction in HP and/or abnormal prefrontal–hippocampal connectivity contributes to the disrupted prefrontal–hippocampal communication. Here, we address this open question by using in utero electroporation (IUE) to knock down DISC1 in CA1 pyramidal neurons of intermediate/ventral HP (i/vHP) during perinatal development in mice exposed to MIA (dual-hit $G_{HP}E$ mice). We combined in vivo electrophysiology with optogenetics to provide direct evidence for the causal contribution of hippocampal pyramidal neurons to the deficits of prefrontal-hippocampal coupling in $G_{HP}E$ mice throughout development.

Materials and Methods

All experiments were performed in compliance with the German laws and the guidelines of the European Community for the use of animals in research and were approved by the local ethical committee (015/17, 015/18). Timed-pregnant C57BL/6 J mice from the animal facility of the University Medical Center Hamburg-Eppendorf were used. The day of vaginal plug detection was defined as gestational day(G) 0.5, whereas the day of birth was defined as postnatal day(P) 0.

Experimental Design

Multisite extracellular recordings and behavioral testing were performed on pups of both sexes during neonatal development (i.e., P8–P10) as well as during prejuvenile development (i.e., P16–P23). None of the investigated parameters differed between males and females, thus, data for both sexes were pooled. In this study, we applied IUE with short-hairpin RNA (shRNA) to DISC1 (5′-GGCAAACACTGTGAAGTGC-3′) under H1 promoter-driven pSuper plasmid to knock down the DISC1 in CA1 of i/vHP. A scrambled target sequence without homology to any known messenger RNA (5′-ATCTCGCTTGGGCGAGAGT-3′) was used as control shRNA. Two genetically engineered mutant mouse models were investigated. First, heterozygous genetically engineered mutant DISC1 mice carrying a Disc1 allele (Disc1Tm1Kara) on a C57BL6/J background were used. Due to two termination codons and a premature polyadenylation site, the allele produces a truncated transcript (Kvajo et al. 2008). Genotypes were determined using genomic DNA and following primer sequences: forward primer 5′-TAGCCACTCTCATTGTCAGC-3′, reverse primer 5′-CCTCATCCCTTCCACTCAGC-3′. DISC1 whole-brain knock-down mice were transfected by IUE with control shRNA+ pAAVCAG-tDimer2 or control shRNA+ pAAV-CAG-ChR2(E123T/T159C)-2A-tDimer2 at G15.5. Control shRNA had no effects on the network activity and prefrontal–hippocampal coupling at neonatal and prejuvenile ages. The resulting offspring mimicking the dual genetic-environmental etiology of mental disorders were classified in GE mice (whole-brain DISC1 knock-down + MIA). Second, C57BL/6J mice with DISC1 knock-down confined to HP were engineered through transfection with DISC1 shRNA. Mice were transfected by IUE with DISC1 shRNA+ pAAVCAG-tDimer2 or DISC1 shRNA+ pAAV-CAG-ChR2(E123T/T159C)-2A-tDimer2 at G15.5. The resulting offspring mimicking the dual genetic-environmental etiology of mental disorders were classified in $G_{HP}E$ mice (hippocampal DISC1 knock-down + MIA). Both two mouse models were challenged by MIA, using the viral mimetic polyinosinic:polycytidylic acid (poly I:C, 5 mg/kg) injected intravenous (i.v.) into the pregnant dams at gestational day G9.5. The offspring of wild-type C57BL/6J

dams injected at G9.5 with saline (0.9%, i.v.) were transfected with control shRNA+pAAV-CAG-tDimer2 or control shRNA+ pAAV-CAG-ChR2(E123T/T159C)-2A-tDimer2 and were classified in control mice (CON).

In Utero Electroporation

Starting 1 day before and until 2 days after surgery, timed-pregnant C57BL/6J mice received on a daily basis additional wet food supplemented with 2–4 drops Metacam (0.5 mg/ml, Boehringer-Ingelheim, Germany). At G15.5, pregnant mice were injected subcutaneously with buprenorphine (0.05 mg/kg body weight) 30 min before surgery. The surgery was performed on a heating blanket and toe pinch and breathing were monitored throughout. Under isoflurane anesthesia (induction: 5%, maintenance: 3.5%), the eyes of the dam were covered with eye ointment to prevent damage before the uterine horns were exposed and moistened with warm sterile phosphate buffered saline (PBS, 37°C). Solution containing 1.25 µg/µL DNA [pAAV-CAG-ChR2(E123T/T159C)-2A-tDimer2, or pAAV-CAG-tDimer2, or shRNA to DISC1 together with pAAV-CAG-tDimer2 (molar ratio = 3:1)] and 0.1% fast green dye at a volume of 0.75–1.25 µL were injected into the right lateral ventricle of individual embryos using pulled borosilicate glass capillaries with a sharp and long tip. Plasmid DNA was purified with NucleoBond (Macherey-Nagel). The 2A encodes for a ribosomal skip sentence, splitting the fluorescent protein tDimer2 from the opsin during gene translation. To target i/vHP, a tri-polar approach was used (Szczurkowska et al. 2016). Each embryo within the uterus was placed between the electroporation tweezer-type paddles (5 mm diameter, both positive poles, Protech) that were oriented at 90° leftward angle from the midline and a 0° angle downward from anterior to posterior. A third custom build negative pole was positioned on top of the head roughly between the eyes. Electrode pulses (30 V, 50 ms) were applied six times at intervals of 950 ms controlled by an electroporator (CU21EX, BEX). By these means, neural precursor cells from the subventricular zone, which radially migrate into the i/vHP CA1 area, were transfected. The expression was confined to HP and no neighboring neocortical areas were transfected. Uterine horns were placed back into the abdominal cavity after electroporation. The abdominal cavity was filled with warm sterile PBS (37°C) and abdominal muscles and skin were sutured individually with absorbable and nonabsorbable suture thread, respectively. After recovery, pregnant mice were returned to their home cages, which were half placed on a heating blanket for 2 days after surgery.

Surgery for In Vivo Electrophysiological Recordings and Light Stimulation

For neonatal (P8–10) recordings in nonanesthetized state, 0.5% bupivacain/1% lidocaine was locally applied on the neck muscles. For prejuvenile (P20–23) recordings under anesthesia, mice were injected intraperitoneally (i.p.) with urethane (1 mg/g body weight; Sigma-Aldrich) prior to surgery. For both age groups, under isoflurane anesthesia (induction: 5%, maintenance: 2.5%), the head of the pup was fixed into a stereotaxic apparatus using two plastic bars mounted on the nasal and occipital bones with dental cement. The bone above the PFC (0.5 mm anterior to bregma, 0.1–0.5 mm right to the midline), HP (3.5 mm posterior to bregma, 3.5 mm right to the midline) was carefully removed by drilling a hole of <0.5 mm in diameter. After a 10 min recovery period on a heating blanket, mouse was placed into the setup

for electrophysiological recording. Throughout the surgery and recording session the mouse was positioned on a heating pad with the temperature kept at 37°C.

Electrophysiological Recordings

A four-shank electrode (NeuroNexus) containing 4 x 4 recording sites (0.4–0.8 MΩ impedance, 100 µm spacing, 125 µm inter-shank spacing) was inserted into the prelimbic (PL) subdivision of PFC. A one-shank optoelectrode (NeuroNexus) containing 1 x 16 recordings sites (0.4–0.8 MΩ impedance, 50 µm spacing) aligned with an optical fiber (105 mm diameter) ending 200 µm above the top recording site was inserted into CA1 area. A silver wire was inserted into the cerebellum and served as ground and reference electrode. Extracellular signals were band-pass filtered (0.1–9000 Hz) and digitized (32 kHz) with a multichannel extracellular amplifier (Digital Lynx SX; Neuralynx) and the Cheetah acquisition software (Neuralynx). Spontaneous (i.e., not induced by light stimulation) activity was recorded for 20 min at the beginning of each recording session as baseline activity. The position of recording electrodes in the PL and CA1 area of i/vHP was confirmed post mortem. Wide field fluorescence images were acquired to reconstruct the recording electrode position in brain slices of electrophysiologically investigated pups and to localize tDimer2 expression in pups after IUE. Only pups with correct electrode and transfection position were considered for further analysis. In PL, the most medial shank was inserted to target layer 2/3, whereas the most lateral shank was located into layer 5/6. For the analysis of hippocampal local field potential (LFP), the recording site located in the pyramidal layer, where sharp waves (SPWs) reverse (Bitzenhofer and Hanganu-Opatz 2014) was selected to minimize any nonstationary effects of large amplitude events. For the analysis of hippocampal firing, two channels above and two channels below the site used for LFP analysis were additionally considered.

Light Stimulation

Pulsatile (laser on–off, 3 ms-long, 8 Hz) or ramp (linearly increasing power, 3 s-long) light stimulations were performed with an arduino uno (Arduino) controlled diode laser (473 nm; Omicron). Laser power was adjusted to trigger neuronal spiking in response to >25% of 3 ms-long light pulses at 8 Hz. Resulting light power was in the range of 20–40 mW/mm^2 at the fiber tip.

Behavioral Experiments

The exploratory behavior and recognition memory of CON, G$_{HP}$E, and GE mice were tested at prejuvenile age (P16–20) using previously established experimental protocols (Kruger et al. 2012). Briefly, all behavioral tests were conducted in a custom-made circular white arena, the size of which (D: 34 cm, H: 30 cm) maximized exploratory behavior, while minimizing incidental contact with testing objects (Heyser and Ferris 2013). The objects used for testing of novelty recognition were six differently shaped, textured and colored, easy to clean items that were provided with magnets to fix them to the bottom of the arena. Object sizes (H: 3 cm, diameter: 1.5–3 cm) were smaller than twice the size of the mouse and did not resemble living stimuli (no eye spots, predator shape). The objects were positioned at 10 cm from the borders and 8 cm from the center of the arena. After every trial the objects and arena were cleaned with 0.1% acetic acid to remove all odors. A black and white CCD camera (VIDEOR TECHNICAL E. Hartig GmbH) was mounted 100 cm above the arena and connected to a PC via PCI interface

serving as frame grabber for video tracking software (Video Mot2 software, TSE Systems GmbH).

Exploratory Behavior in the Open Field

Mice (P15) were habituated to the arena by freely exploring the arena during two 10-min sessions 1 day before the OF task. The next day, mice (P16) were allowed to freely explore the testing arena for 10 min. Additionally, the floor area of the arena was digitally subdivided in 8 zones (4 center zones and 4 border zones) using the zone monitor mode of the VideoMot 2 analysis software (VideoMot 2, TSE Systems GmbH). The time spent by pups in center and border zones, as well as the running distance and velocity were quantified.

Novelty Recognition Paradigms

All protocols for assessing item recognition memory in P17 mice consisted of familiarization and testing trials (Ennaceur and Delacour 1988). In the novel object recognition (NOR) task, during the familiarization trial each mouse was placed into the arena containing two identical objects and released against the center of the opposite wall with the back to the objects. After 10 min of free exploration of objects, the mouse was returned to a temporary holding cage. Subsequently, the test trial was performed after a delay of 5 min postfamiliarization. The mice were allowed to investigate one familiar and one novel object with a different shape and texture for 5 min. Since some mice lost interest to achieve the tasks even before the end of investigation time, object interaction during the first 3 min was analyzed and compared between the groups. Discrimination ratio was calculated as (time spent interacting with novel object – time spent interacting with the familiar object)/(time spent interacting with novel object + time spent interacting with the familiar object).

In the recency recognition (RR) task, tested at P19–20, mice experienced two 10 min-long familiarization trials with two different sets of identical objects that were separated by a delay of 30 min. The second familiarization trial was followed after 5 min by a test trial in which one object used in the first and one object used in the second more recent familiarization trial were placed in the arena at the same positions as during the familiarization trials. Object interaction during the first 3 min was analyzed and compared between the groups. All trials were video-tracked and the analysis was performed using the Video Mot2 analysis software. The object recognition module of the software was used and a three-point tracking method identified the head, the rear end and the center of gravity of the mouse. Digitally, a circular zone of 1.5 cm was created around each object and every entry of the head point into this area was considered as object interaction. Climbing or sitting on the object, mirrored by the presence of both head and center of gravity points within the circular zone, were not counted as interactions. Discrimination ratios were calculated as (time spent interacting with more recent object – time spent interacting with less recent object)/(time spent interacting with more recent object + time spent interacting with less recent object).

Histology and Immunohistochemistry

Histological procedures were performed as previously described (Bitzenhofer et al. 2017b; Oberlander et al. 2019; Xu et al. 2019). Briefly, P8–10 and P20–23 mice were anesthetized with 10% ketamine (aniMedica)/2% xylazine (WDT) in 0.9% NaCl solution (10 μg/g body weight, i.p.) and transcardially perfused

with Histofix (Carl Roth) containing 4% paraformaldehyde. Brains were postfixed in Histofix for 24 h and sectioned coronally at 50 mm (immunohistochemistry) or 100 mm (Sholl and spine analysis). Free-floating slices were permeabilized and blocked with PBS containing 0.8% Triton X 100 (Sigma-Aldrich), 5% normal bovine serum (Jackson Immuno Research) and 0.05% sodium azide. Subsequently, slices were incubated with mouse monoclonal Alexa Fluor-488 conjugated antibody against NeuN (1:200, MAB377X, Merck Millipore) or the rabbit polyclonal primary antibody against DISC1 (1:250, 40–6800, Thermo Fisher Scientific), followed by 2 h incubation with Alexa Fluor-488 goat anti-rabbit IgG secondary antibody (1:500, A11008, Merck Millipore). Slices were transferred to glass slides and covered with Fluoromount (Sigma-Aldrich). Wide-field fluorescence images were acquired to reconstruct the recording electrode position and the location of tDimer2 expression. High-magnification images were acquired by confocal microscopy (DM IRBE, Leica) to quantify DISC1 expression. For this, the fluorescence intensity of DISC1 in tDimer2-positive neurons was calculated. All images were similarly processed and analyzed using ImageJ software.

Neuronal Morphological Analysis

Microscopic stacks were examined on a confocal microscopy (DM IRBE, Leica Microsystems, Zeiss LSN700). Stacks were acquired as 2048×2048 pixel images (pixel size, 78 nm; Z-step, 500 nm). Sholl analysis and spine density quantification were carried out in the ImageJ environment. For Sholl analysis, images were binarized (auto threshold) and dendrites were traced using the semiautomatical plugin *Simple Neurite Tracer*. The traced dendritic tree was analyzed with the plugin Sholl Analysis, after the geometric center was identified using the blow/lasso tool. For spine density quantification, the length (line) and number of spines (point picker) on the dendrite of interest (apical, basal, proximal oblique, or secondary apical) were quantified.

Data Analysis

Data were imported and analyzed offline using custom-written tools in MATLAB software version 7.7 (Mathworks). The data were processed as following: (i) band-pass filtered (500–5000 Hz) to detect multiple-unit activity (MUA) as negative deflections exceeding five times the standard deviation of the filtered signals and (ii) low-pass filtered (<1500 Hz) using a third-order Butterworth filter before downsampling to 1000 Hz to analyze the LFP. All filtering procedures were performed in a phase-preserving manner. The position of DiI-stained recording electrodes in PL (most medial shank confined to layer 2/3, most temporal shank confined to layer 5/6) and CA1 was confirmed postmortem by histological evaluation. Additionally, electrophysiological features (i.e., reversal of LFP and high MUA frequency over stratum pyramidale of CA1) were used for confirmation of the exact recording position in HP.

Detection of neonatal oscillatory activity. Discontinuous oscillatory events were detected using a previously developed unsupervised algorithm (Cichon et al. 2014) and confirmed by visual inspection. Briefly, deflections of the root-mean-square of band-pass (3–100 Hz) filtered signals exceeding a variance-depending threshold were assigned as network oscillations. The threshold was determined by a Gaussian fit to the values ranging from 0 to the global maximum of the root-mean-square histogram. Only oscillatory events > 1 s were considered for further analysis.

Time–frequency plots were calculated by transforming the data using the Morlet continuous wavelet.

Power Spectral Density
For power spectral density analysis, 1 s-long windows of network oscillations were concatenated and the power was calculated using Welch's method with nonoverlapping windows. For optical stimulation, we compared the average power during the 1.5 s-long time window preceding the stimulation to the last 1.5 s-long time window of light-evoked activity.

Single Unit Activity
Single unit activity (SUA) was detected and clustered using klusta (Rossant et al. 2016) and manually curated using phy (https://github.com/cortex-lab/phy). Data were imported and analyzed using custom-written tools in the MATLAB.

Firing Rate
The firing rate was computed by dividing the total number of spikes by the duration of the analyzed time window.

Interspike Interval
ISI was calculated at 1 ms resolution in the range of 10–200 ms.

Spike-Triggered LFP Power
Excitatory inputs arriving from a presynaptic cell generate excitatory postsynaptic potentials (EPSPs) in the postsynaptic cell. The spike-triggered LFP power was calculated to estimate the effects of the EPSPs on the LFP. Spike-triggered LFP spectra were calculated as

$$\left(\text{Power}_{\text{spike}} - \text{Power}_{\text{baseline}}\right) / \text{Power}_{\text{baseline}}$$

where the spike-triggered power spectrum ($\text{Power}_{\text{spike}}$) was calculated using Welch's method for a 200 ms-long time window centered on each spike, and the power spectrum of baseline LFP ($\text{Power}_{\text{baseline}}$) was averaged for two time windows, 100–300 ms and 200–400 ms before each spike.

Detection of SPWs in HP
The filtered signal (1–300 Hz) was subtracted from the signal recorded 100 µm above and 100 µm below stratum pyramidale. SPWs were detected as peaks above five times the standard deviation of the subtracted signal.

Phase Locking Value
Phase locking value (PLV) is developed to analyze the strength of phase synchronization. The analytic phase has a clear meaning only at a narrow frequency band. Therefore, the signal was first filtered into a narrow frequency band (bandwidth = 1 Hz, step = 1 Hz, for example 1–2 Hz, 2–3 Hz, ..., 49–50 Hz) in a phase preserving manner. Then, Hilbert transform was applied to extract the phase of the two signals. PLV was defined as following,

$$\text{PLV} = \left|\text{mean}\ \left(\exp\left(i * \Delta \varnothing_t\right)\right)\right|$$

with $\Delta \varnothing_t$ stands for phase difference between the two signals at time point t. The value of PLV ranged between 0 (no synchrony) and 1 (max synchrony).

Spectral Coherence
Coherence was calculated using the coherency method. Briefly, the coherence was calculated (using Matlab build-in functions cpsd.m and pwelch.m) by cross-spectral density between the two signals and normalized by the power spectral density of each. The computation of the coherence C over frequency (f) for the power spectral density P of signal X and Y was performed according to the formula:

$$C_{XY}(f) = \left|\left(\frac{P_{XY}(f)}{\sqrt{P_{XX}(f)P_{YY}(f)}}\right)\right|$$

Directionality Methods
To investigate the directionality of functional connectivity between PFC and HP, generalized partial directed coherence (gPDC) was used. gPDC is based on linear Granger causality measure in the frequency domain. The method attempts to describe the causal relationship between multivariate time series based on the decomposition of multivariate partial coherence computed from multivariate autoregressive models. The LFP signal was divided into 1 s-long segments containing the oscillatory activity. After de-noising using MATLAB wavelet toolbox, gPDC was calculated using a previously described algorithm (Baccala and Sameshima 2001; Baccala et al. 2007).

Estimation of Light Propagation
The spatial pattern of light propagation in vivo was estimated using a previously developed model (Stujenske et al. 2015) based on Monte Carlo simulation (probe parameters: light fiber diameter: 50 µm, numerical aperture: 0.22, light parameters: 594 nm, 0.6 mW).

Pearson's correlation
For correlation between gPDC and NOR/RR, we computed Pearson's correlation using *corrplot.m* in MATLAB.

Generalized Linear Model
GLM was performed to predict the animals' behavioral performance in NOR and RR tasks by gPDC. Group comparisons were performed with GLM by including the factor of group as predictor variable.

Statistical Analysis
Statistical analyses were performed in MATLAB environment. Significant differences were detected by paired t-test or one-way ANOVA followed by Bonferroni-corrected post hoc analysis. For Sholl analysis, one-way repeated-measures ANOVA was used. Investigators were blinded to the group allocation when Sholl and spine analyses were performed. Data are presented as mean ± sem. Significance levels of $P < 0.05$ (*), $P < 0.01$ (**), or $P < 0.001$ (***) were tested. Statistical parameters can be found in the main text, tables, and/or in the figure legends.

Results

Whole-Brain DISC1 Knock-Down in Immune-Challenged Mice Perturbs the Patterns of Network and Spiking Activity in Neonatal Intermediate/Ventral HP

Developing prefrontal–hippocampal circuits have been shown to be highly sensitive to the detrimental impact of combined

genetic defects and environmental stressors, whereas single-hit that have been previously characterized in detail at neonatal and juvenile age had no abnormal phenotype (Hartung et al. 2016; Oberlander et al. 2019). These results contrast with the prominent effects of DISC1- and MIA-only in adult mice that have network dysfunction and cognitive deficits (Kvajo et al. 2008, 2011; Abazyan et al. 2010; Cash-Padgett and Jaaro-Peled 2013b; Lipina et al. 2013; Sauer et al. 2015).

The mechanisms of abnormal long-range communication and wiring in dual-hit mice are still largely unknown. One possibility is that the maturation of PFC is impaired and therefore, the excitatory drive from the HP does not succeed to entrain the local circuits in beta–gamma frequencies. Indeed, we recently proved that this is a mechanism of developmental dysfunction (Xu et al. 2019; Chini et al. 2020). A second mechanism might be that the hippocampal driving force is decreased as result of abnormal function of developing hippocampal circuits in dual-hit mice.

To test the second hypothesis, we firstly characterized in detail the hippocampal patterns of network and firing activity in immune-challenged mice with whole-brain DISC1 knock-down. For this, we performed extracellular recordings of LFP and MUA from the CA1 area of i/vHP of awake P8–10 CON ($n = 22$) and GE ($n = 19$) mice (Fig. 1A). As previously reported (Brockmann et al. 2011), discontinuous spindle-shaped oscillations with frequency components peaking in theta band (4–12 Hz) intermixed with irregular low amplitude beta–gamma band components (12–50 Hz) are the dominant pattern of network activity in the CA1 area of both mouse groups (Fig. 1B). However, their properties significantly differed between CON and GE mice, conferring a highly fragmented appearance of hippocampal oscillations in GE mice (Fig. 1C,D). Their duration of oscillatory events was significantly shorter in GE mice (CON: 4.46 ± 0.24 s, GE: 3.38 ± 0.18 s, $F(1,39) = 13.31$, $P = 7.7^{*}10^{-4}$, one-way ANOVA) at a comparable occurrence (CON: 8.7 ± 0.30 oscillations/min, GE: 9.47 ± 0.38 oscillations/min, $F(1,39) = 2.44$, $P = 0.126$, one-way ANOVA) (Fig. 1C). Their spectral composition (4–50 Hz) differed between groups, the GE mice having hippocampal events with weaker power when compared to CON (4–50 Hz, $F(1,39) = 4.29$, $P = 0.045$, one-way ANOVA) (Fig. 1D). The overall firing of single neurons in the hippocampal CA1 area of CON and GE was similar both in its rate (log of firing rate, CON: -0.53 ± 0.29; GE: -0.48 ± 0.39; $F(1,39) = 0.009$, $P = 0.924$, one-way ANOVA) and temporal organization (i.e., preferred interspike interval [ISI] of 125 ms, corresponding to 8 Hz) (Fig. 1E,F).

Besides spindle-shaped oscillations, prominent SPWs reversing across the pyramidal layer have been recorded in the neonatal CA1 area of CON and GE mice (Fig. 1G). They were accompanied by ripples (100–250 Hz) and prominent firing. GE mice had fewer SPWs (0.36 ± 0.02 Hz, $F(1,39) = 4.38$, $P = 0.043$, one-way ANOVA) when compared with CON mice (0.41 ± 0.02 Hz) (Fig. 1H). The SPW-related spiking also decreased (CON: 0.76 ± 0.08 Hz, GE: 0.47 ± 0.09, $F(1,37) = 6.02$, $P = 0.019$, one-way ANOVA) (Fig. 1I,J). The rather moderate perturbation of theta oscillations, which have been shown to mainly originate outside CA1 area (Buzsaki 2002; Janiesch et al. 2011), and the prominent deficits of locally generated SPWs and related spiking suggest that the i/vHP is compromised in GE mice. Analysis of the position and density of pyramidal neurons suggests that delayed migration of these neurons and correspondingly, perturbed wiring of local circuits, account for the hippocampal dysfunction (Fig. 1K).

These data indicate that neonatal HP is impaired in dual-hit genetic-environmental models of disease.

DISC1 Knock-Down in Hippocampal Pyramidal Neurons Disturbs the Prefrontal Oscillatory Activity and Prefrontal–Hippocampal Coupling of Neonatal Immune-Challenged Mice

When brain-wide expressed, genetic abnormalities, such as DISC1 knock-down in immune-challenged mice may affect many-fold the communication between limbic areas. To selectively pinpoint their role for hippocampal function, we generated $G_{HP}E$ mice in which the DISC1 knock-down was restricted to a lineage of pyramidal neurons in hippocampal CA1 area. For this, we expressed a DISC1 targeting shRNA in the CA1 of the i/vHP by using IUE protocols previously described (Ahlbeck et al. 2018). CON and GE mice received a scrambled/control shRNA instead (Fig. 2A). The immune challenge in $G_{HP}E$ and GE mice, which has been identified as critical cofactor of impairment (Hartung et al. 2016; Oberlander et al. 2019), was mimicked by MIA with the viral mimetic poly I:C injected at gestational day 9.5. In contrast, CON mice received saline injections at the same age. Staining for NeuN showed that a similar fraction of neurons was transfected in CON ($21.89 \pm 0.02\%$; $n = 6$), $G_{HP}E$ ($20.80 \pm 0.01\%$; $n = 6$) and GE mice ($20.59 \pm 0.02\%$; $n = 6$) (Fig. 2B). The shape of tDimer2-positive neurons and the orientation of primary dendrites confirmed previous findings (Ahlbeck et al. 2018) that the transfection was restricted to cell lineages of pyramidal neurons. In $G_{HP}E$, DISC1 was efficiently suppressed by shRNA (Fig. 2C). The relative DISC1 intensity in CA1 area was significantly weaker ($F(1,142) = 321.51$, $P = 1.06^{*}e\text{-}10$, one-way ANOVA) in neonatal $G_{HP}E$ (40.98 ± 2.56) when compared with CON (101.74 ± 2.14) mice (Fig. 2C).

To monitor the effects of DISC1 knock-down in the i/vHP, we performed extracellular recordings of LFP and MUA from HP of P8–P10 awake CON ($n = 22$), $G_{HP}E$ ($n = 15$), and GE mice ($n = 19$). Similar to GE mice, $G_{HP}E$ mice showed disorganized oscillatory activity in CA1 area with decreased duration and theta–beta band power (4–50 Hz) but unchanged occurrence of spindle-shaped oscillations (Table 1, Fig. 2D,E). HP-confined DISC1 knock-down caused reduced SPWs occurrence and SPW-related neuronal firing, similarly to the deficits described for GE mice (Table 1, Fig. 2F,G).

In light of these findings, the question arises, whether the hippocampal dysfunction in $G_{HP}E$ mice is sufficient to affect downstream brain areas with normal DISC1 expression, such as PL. To answer this question, we performed extracellular recordings of LFP and MUA from PL of P8–P10 awake CON ($n = 22$), $G_{HP}E$ ($n = 15$), and GE mice ($n = 19$) using four shanks recording electrodes spanning the prelimbic layers 2/3 and 5/6 (Fig. 2H). In line with previous investigations (Hartung et al. 2016; Chini et al. 2020), the PL of all investigated mice showed discontinuous spindle-shape oscillations with frequencies ranging from theta to beta-low gamma range (20–40 Hz). While the occurrence of these events was similar across the three groups, their duration and power were decreased in GE and $G_{HP}E$ mice when compared with CON mice (Table 1, Fig. 2I,J). As previously reported (Chini et al. 2020), brain-wide DISC1 knock-down in combination with MIA significantly lowered the neuronal firing in prelimbic layer 2/3. In contrast, $G_{HP}E$ mice showed normal firing in both layers 2/3 and 5/6 (Table 1, Fig. 2K) that might result from the sparse hippocampal innervation targeting the PFC. The decreased network entrainment and unchanged firing in PL of $G_{HP}E$ mice suggest that the local prelimbic circuits are indirectly impaired, most likely through a weaker drive from HP, which at this age is the main source of PL activation (Brockmann et al. 2011; Ahlbeck
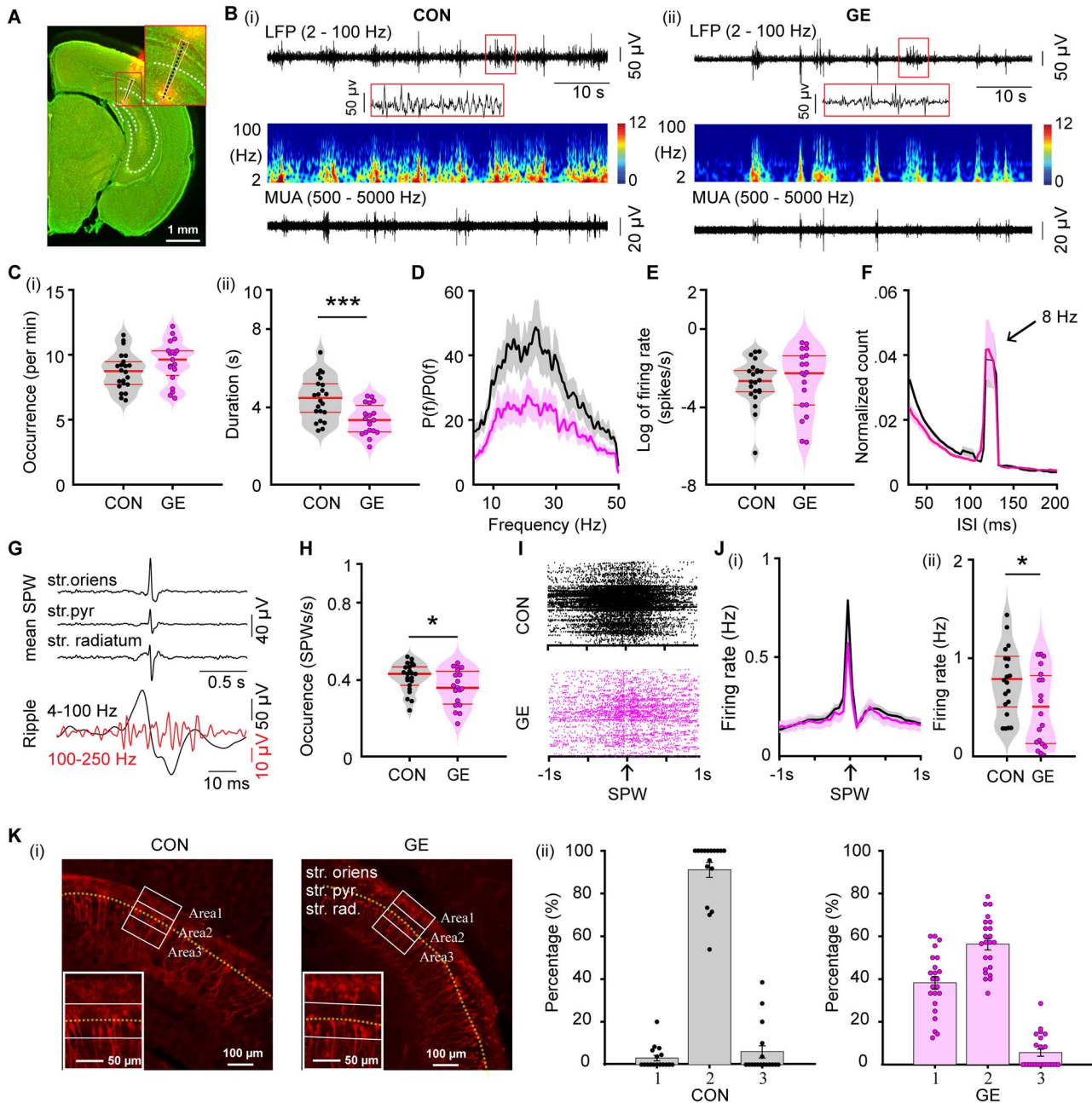
Figure 1. Patterns of network activity and neuronal firing in the CA1 area of i/vHP from neonatal GE mice. (A) Digital photomontage reconstructing the location of the DiI-labeled 1×16-site recording electrode (orange) in a 100 μm-thick coronal section containing the CA1 from a P9 mouse. Inset, the position of recording sites (black dots) over the pyramidal layers displayed at higher magnification. (B) Extracellular LFP recordings of discontinuous oscillatory activity in the CA1 area from a P9 CON (i) and a P9 GE (ii) mouse displayed after bandpass (2–100 Hz) filtering (top) and the corresponding MUA after bandpass (500–5000 Hz) filtering (bottom). Traces are accompanied by the color-coded wavelet spectra of the LFP at identical time scale. (C) Violin plots displaying the occurrence (i) and the duration (ii) of hippocampal oscillatory activity recorded in CON and GE mice. (D) Averaged power spectra P(f) of discontinuous oscillatory activity normalized to the baseline power P0(f) of time windows lacking oscillatory activity in CON (black) and GE (red) mice. (E) Violin plots displaying the firing activity of CA1 neurons in CON and GE mice. (F) Histograms of ISI for CON (black) and GE (red) mice. Note the prominent ISI peak at ∼125 ms interval, which corresponds to ∼8 Hz. (G) Characteristic SPWs and ripple events recorded in the CA1 area. (H) Violin plots displaying the occurrence of SPWs in CON and GE mice. (I) Examples of spike trains from CA1 neurons aligned to SPWs in CON and GE mice. (J) Histograms of spiking activity aligned to SPWs (i) and violin plots displaying peak firing rate at SPWs (ii) in CON (black) and GE (red) mice. (K) (i) Photomicrographs depicting tDimer2-expressing pyramidal neurons (red dots) in the CA1 area of a P9 CON mouse and a P9 GE mouse. The yellow dotted line indicates the pyramidal layer of CA1. The three white blocks with width of 80 μm and length of 200 μm centered on the pyramidal layers correspond to the regions of interest for the quantification of tDimer-transfected neurons. Inset, the tDimer2-expressing cells over the pyramidal layers displayed at higher magnification. (ii) Bar diagram of the distribution of the tDimer-transfected neurons in the three blocks defined in (i) in CON and GE mice. Single data points are represented as dots. Single data points are represented as dots and the red horizontal bars in violin plots correspond to the median and the 25th and 75th percentiles. *P < 0.05, ***P < 0.001.
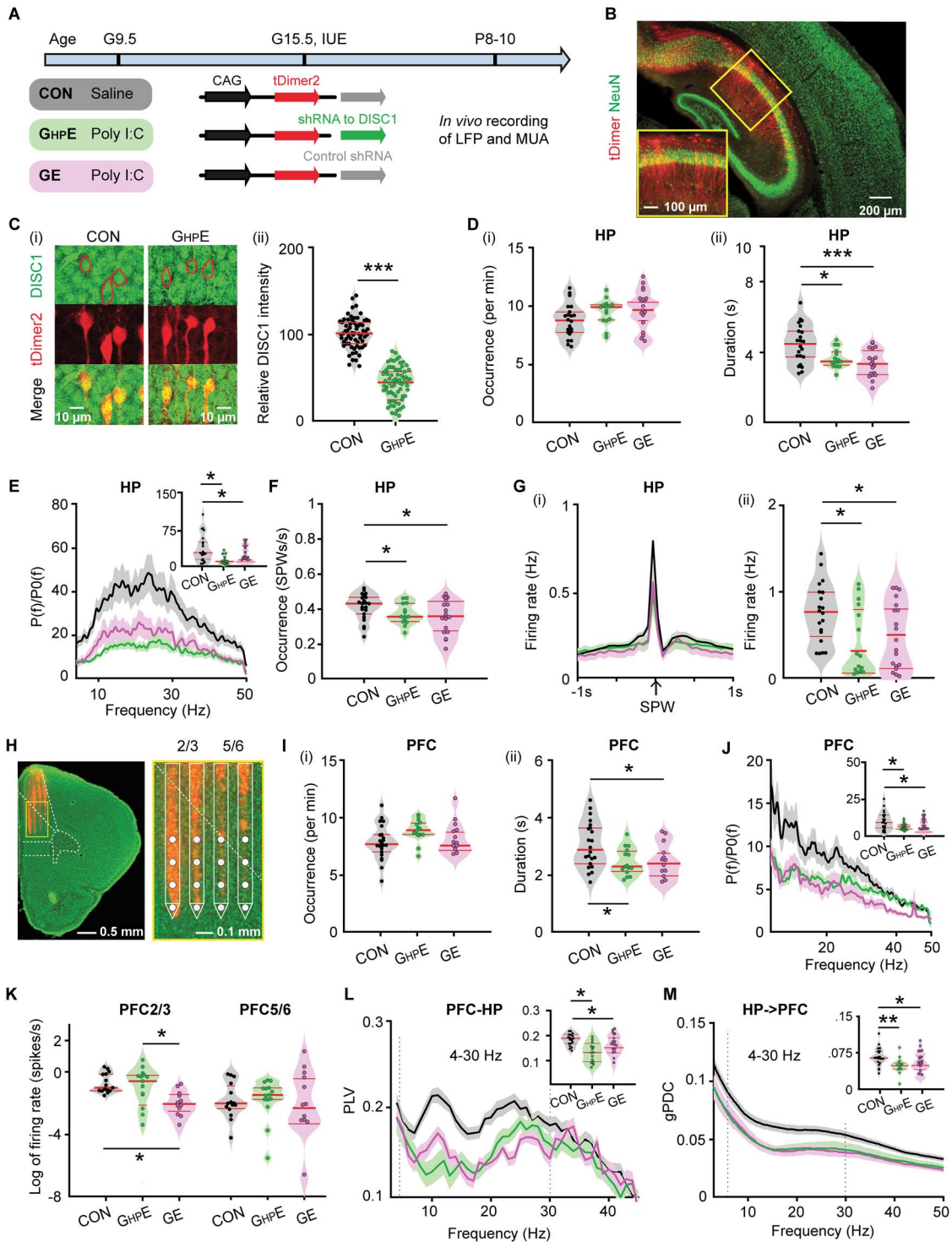
Figure 2. Patterns of network activity and neuronal firing in HP and PFC from neonatal immune challenged mice with HP-confined DISC1 suppression. (A) Timeline of experimental protocol and description of the three investigated groups of mice: CON mice, immune-challenged mice with suppression of DISC1 confined to HP (G$_{HP}$E), and immune-challenged mice with brain-wide DISC1 knock-down (GE). For each group the constructs used for IUE to target hippocampal CA1 pyramidal neurons is specified. (B) Photomicrographs depicting tDimer2-expressing pyramidal neurons (red) in the CA1 area when stained for NeuN (green) from a P9 mouse. Inset, photograph displaying the tDimer2-expressing cells at a higher magnification. (C) (i) Photographs displaying the DISC1 immunoreactivity (green) in relationship with the tDimer2-expression (red) in the CA1 area of i/vHP from P9 G$_{HP}$E and CON mice. (ii) Violin plots displaying the relative DISC1 immunoreactivity averaged for G$_{HP}$E and CON mice at P8-P10. (D) Violin plots displaying the occurrence (i) and the duration (ii) of hippocampal oscillatory activity recorded in CON, G$_{HP}$E and GE mice. (E) Averaged power spectra P(f) of discontinuous oscillatory activity normalized to the baseline power P0(f) of time windows lacking oscillatory activity in CON (black), G$_{HP}$E (green), and GE (magenta) mice. Insert, violin plots displaying the relative power averaged for 4–50 Hz in CON, G$_{HP}$E, and GE mice. (F) Violin plots displaying the occurrence of SPWs in the CA1 area of CON, G$_{HP}$E, and GE mice. (G) Histograms of spiking activity aligned to SPWs (i) and violin plots displaying the peak SPW-related firing in CON (black), G$_{HP}$E (green), and GE (magenta) mice (ii). (H) Left, digital photomontage reconstructing the location of the DiI-labeled 4 × 4-site recording electrode

et al. 2018). To test this hypothesis, we firstly assessed the synchrony between PL and HP in CON ($n = 22$), $G_{HP}E$ ($n = 15$), and GE mice ($n = 19$) by calculating PLV that, relying on oscillatory phase information, are not biased by different amplitudes of activity in PFC and HP. In line with previous data (Hartung et al. 2016; Xu et al. 2019), a tight theta–beta band (4–30 Hz) coupling of spindle-bursts between PL and HP has been detected in neonatal CON mice. In contrast, the PLV was significantly lower in $G_{HP}E$ and GE mice ($F(2, 51) = 4.20$, $P = 0.021$, one-way ANOVA) (Table 1, Fig. 2L). The directionality of interactions between PL and HP was also affected by both brain-wide and HP-confined DISC1 knock-down in immune-challenged mice. Calculation of gPDC, a measure that reflects the directionality of network interactions in different frequency bands, confirmed the prominent drive from HP to PL. In both GE and $G_{HP}E$, this drive decreased within 4–30 Hz frequencies (Table 1, Fig. 2M). These results give first evidence that the suppression of DISC1 restricted to HP has detrimental effects on the function of downstream PL. This dysfunction is the result of combined genetic and environmental stressors, since neither DISC- nor MIA-only causes major impairment of prefrontal–hippocampal circuits at neonatal age (Hartung et al. 2016; Oberlander et al. 2019).

Hippocampal Dysfunction Through DISC1 Suppression is Sufficient to Reduce the Oscillatory Entrainment of PL and Prelimbic-Hippocampal Coupling in Neonatal Immune-Challenged Mice

To add causal evidence to the hypothesis that the hippocampal dysfunction is critical for the abnormal coupling between PL and HP, we selectively transfected the hippocampal pyramidal neurons in CON, $G_{HP}E$ and GE mice with a highly efficient fast-kinetics double mutant ChR2E123T/T159C (ET/TC) (Berndt et al. 2011) and the red fluorescent protein tDimer2 by IUE (Fig. 3A). For $G_{HP}E$ mice, constructs coding for ChR2E123T/T159C (ET/TC) were transfected together with shRNA to DISC1. For targeting i/vHP, a previously developed protocol for IUE using three paddles was used (Szczurkowska et al. 2016; Ahlbeck et al. 2018). This method enables stable area and cell type-specific transfection of hippocampal neurons already prenatally without the need of cell-type specific promotors of a sufficiently small size (Baumgart and Grebe 2015; Szczurkowska et al. 2016) (Fig. 3Bi). The expression rate and distribution of tDimer2-positive neurons within the iso-contour lines for light power of 1 mW/mm^2 were similar in CON ($0.134 \pm 0.009/1000$ μm^2, $n = 16$), $G_{HP}E$ ($0.127 \pm 0.008/1000$ μm^2, $n = 15$) and GE ($0.126 \pm 0.010/1000$ μm^2, $n = 18$) ($F(2, 46) = 0.224$, $P = 0.800$, one-way ANOVA) (Fig. 3Bii). As previously shown, the transfection procedure had no effects on the overall development of mice (weight, somatic development, reflexes) (Ahlbeck et al. 2018).

First, we assessed the efficiency of light stimulation in evoking action potentials in hippocampal pyramidal neurons in vivo.

For this, we stimulated the i/vHP with pulsed blue light (473 nm, 20–40 mW/mm^2) at 8 Hz, since this frequency has been shown to optimally drive the PL (Ahlbeck et al. 2018). The used light power did not cause local tissue heating that might interfere with neuronal spiking (Stujenske et al. 2015; Bitzenhofer et al. 2017a). In all three mouse groups, light stimulation induced precisely timed firing (latency < 10 ms) of CA1 neurons (Fig. 3C).

Second, to investigate the effects of hippocampal activation on downstream prelimbic circuits, we performed extracellular recordings of LFP in the PL during pulsed light stimulation of CA1 area in CON ($n = 15$), $G_{HP}E$ ($n = 18$), and GE ($n = 15$) mice (Fig. 3D). In CON mice, the light-induced hippocampal firing significantly augmented the prefrontal oscillatory activity in all frequency bands, as reflected by the higher power during stimulation when compared with the time window before the train of pulses (Table 2, Fig. 3D). In contrast, the light-induced hippocampal firing failed to boost the prelimbic oscillatory activity in $G_{HP}E$ and GE mice (Fig. 3D).

The weaker hippocampal drive to PL in $G_{HP}E$ mice might result from abnormal network entrainment of the i/vHP. To test this hypothesis, we applied ramp stimulations that, in contrast to light pulses, trigger more physiological firing and do not induce power contamination by repetitive and large voltage deflections (Bitzenhofer et al. 2017a). Ramp stimulation (3 s duration) of CA1 neurons led to sustained increase of spike discharge and augmented theta–beta oscillatory power in the HP of CON mice (Table 2, Fig. 3E). These effects were absent in GE and $G_{HP}E$ mice. Moreover, despite similar hippocampal firing responsiveness to light stimuli, the ability of CA1 neurons contributing to network oscillations in beta–gamma frequencies (20–40 Hz) dramatically decreased in GE and $G_{HP}E$ mice as shown by the weaker spike-triggered LFP relative power (Table 2, Fig. 3G).

Consistent with the excitatory drive from HP to PL during neonatal development, ramp stimulation-induced CA1 firing was relayed to PL and caused augmentation of prelimbic firing across layers in all investigated mouse groups (Fig. 3H). Since the axonal projections of CA1 neurons target prelimbic layer 5/6 neurons, the firing increase in these layers was stronger than in the layer 2/3 (2.97 ± 0.31 vs. 1.52 ± 0.25, $F(1, 16) = 14.75$, $P = 0.0014$, one-way ANOVA), yet lacked temporal coordination in all mice (see Supplementary Fig. 1Ai,ii). In contrast, the firing within prelimbic layer 2/3 in CON induced by ramp stimulation of CA1 pyramidal neurons had a preferred ISI of ~60 ms, equivalent to a population firing at 16.7 Hz (Fig. 3Ii). Correspondingly, the HP spike-triggered prelimbic layer2/3 LFP relative power peaked at similar frequencies (Fig. 3Iii). These peaks were absent in GE and $G_{HP}E$ mice, reflecting abnormal entrainment of prelimbic circuits. Significant power peak of spike-triggered LFP in prelimbic layer 5/6 was detected in none of the three groups (see Supplementary Fig. 1Aiii). Moreover, ramp-induced activation of CA1 pyramidal neurons boosted the synchrony between PL and HP in CON mice in a frequency-specific manner (peak at

(orange) in a 100 μm-thick coronal section containing the PFC from a P9 mouse. Right, the position of recording sites (white dots) over the prelimbic layers displayed at higher magnification. (I) Violin plots displaying the occurrence (i) and the duration (ii) of prefrontal oscillatory activity recorded in CON, $G_{HP}E$, and GE mice. (J) Averaged power spectra $P(f)$ of discontinuous oscillatory activity normalized to the baseline power $P0(f)$ of time windows lacking oscillatory activity in CON (black), $G_{HP}E$ (green), and GE (magenta) mice. Inset, violin plots displaying the relative power averaged for 4–50 Hz in CON, $G_{HP}E$ and GE mice. (K) Violin plots displaying the neuronal firing in prefrontal layer 2/3 and layer 5/6 of CON, $G_{HP}E$, and GE mice. Each dot stands for one slice (3–4 slices per mouse). (L) Line plots of mean PLV for oscillatory activity simultaneously recorded in PFC and HP of in CON (black), $G_{HP}E$ (green), and GE (magenta) mice. Inset, violin plots displaying the PLV when averaged for 4–30 Hz. (M) Line plots of mean gPDC in relationship to frequency for HP→PFC in CON (black), $G_{HP}E$ (green), and GE (magenta) mice. Inset, violin plots displaying gPDC when averaged for 4–30 Hz in CON, $G_{HP}E$, and GE mice. Single data points are represented as dots and the red horizontal bars in violin plots correspond to the median and the 25th and 75th percentiles. *$P < 0.05$, **$P < 0.01$, ***$P < 0.001$.
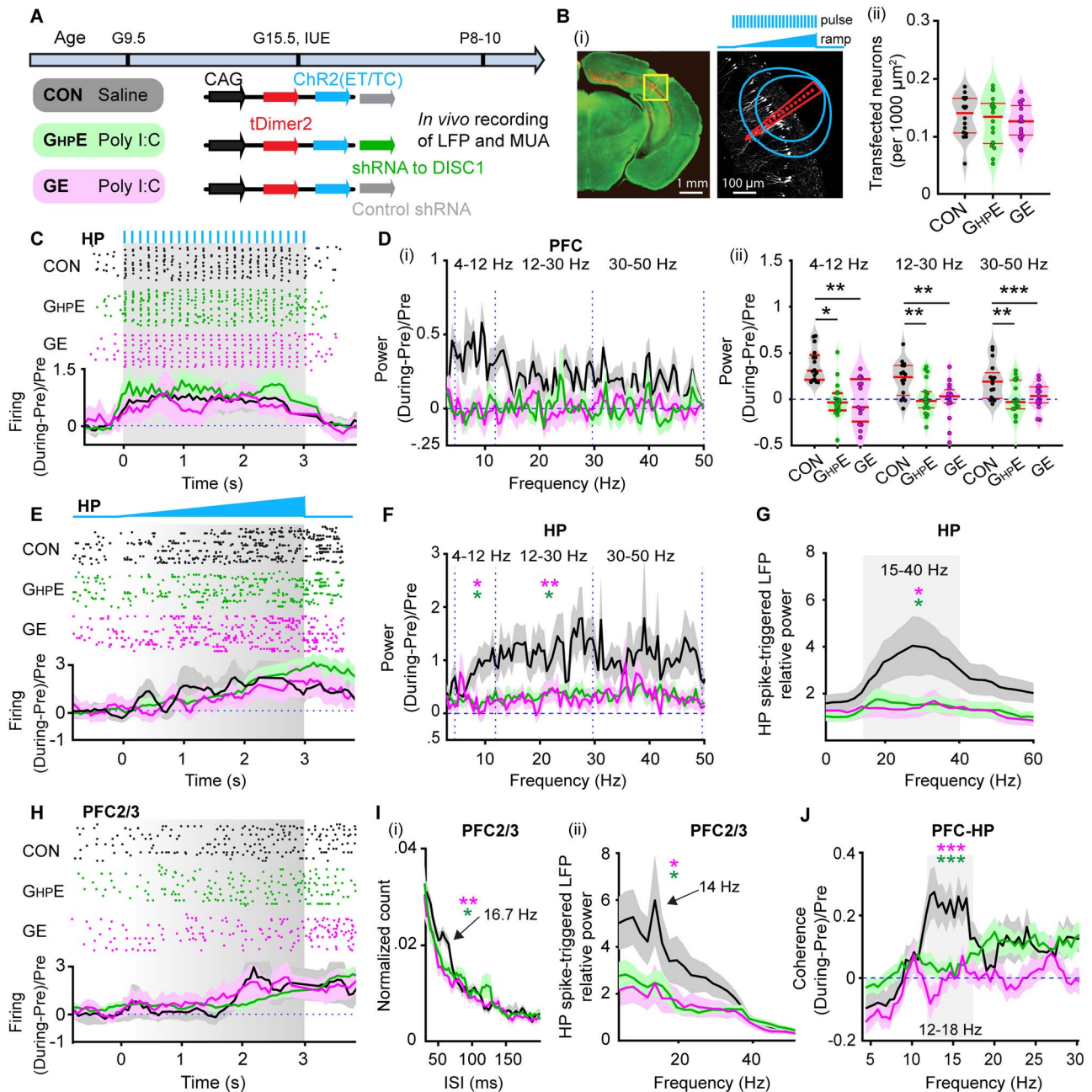
Figure 3. Light-induced activation of i/vHP and prefrontal–hippocampal coupling in immune challenged mice with whole-brain and HP-confined DISC1 suppression. (A) Timeline of experimental protocol and description of the three investigated groups of mice: CON, $G_{HP}E$, and GE. For each group, the constructs used for IUE to target hippocampal CA1 pyramidal neurons is specified. (B) (i) Left, ChR2(ET/TC)-tDimer2-expressing cells (red) in a 50 µm-thick Nissl-stained (green) coronal section including CA1 area from a P9 mouse. Right, recording sites together with transfected neurons (white dots). Green lines correspond to the iso-contour lines for light power of 1 and 10 mW/mm², respectively. 3 s-long pulse (8 Hz) and ramp stimulation are applied to activate hippocampal pyramidal neurons. (ii) Violin plots displaying the number of transfected neurons within the iso-contour lines for light power of 1 mW/mm². (C) Top, representative raster plot of hippocampal SUA in response to 8 Hz pulse stimulation (3 ms-long pulse, 473 nm) in the CA1 area of P9 CON, $G_{HP}E$, and GE mice. Bottom, Histograms of hippocampal firing activity during 8 Hz pulse stimulation normalized to the activity before stimulation in CON (black), $G_{HP}E$ (blue), and GE (red) mice. (D) (i) Power of prefrontal oscillatory activity during pulse stimulation of CA1 pyramidal neurons normalized to the activity before stimulation in CON (black), $G_{HP}E$ (green), and GE (magenta) mice. (ii) Violin plots displaying the oscillatory power averaged for different frequency bands (4–12 Hz, 12–30 Hz, 30–50 Hz) in response to pulse stimulation for all investigated mice. (E) Top, representative raster plot of hippocampal spiking in response to ramp stimulation (3 s duration, 473 nm) in CON, $G_{HP}E$, and GE mice. Bottom, Histograms of hippocampal firing activity during ramp stimulation normalized to the activity before stimulation in CON (black), $G_{HP}E$ (green), and GE (magenta) mice. (F) Power of hippocampal oscillatory activity during ramp stimulation of CA1 pyramidal neurons normalized to the activity before stimulation in CON (black), $G_{HP}E$ (green), and GE (magenta) mice. (G) Line plots of frequency-dependent relative power of spike-triggered LFP in HP of CON (black), $G_{HP}E$ (green), and GE (magenta) mice. (H) Top, representative raster plot of prefrontal spiking in response to ramp stimulation (3 s duration, 473 nm) in HP in one CON, $G_{HP}E$, and GE mouse. Bottom, histograms of prefrontal firing activity during ramp stimulation normalized to the activity before stimulation in CON (black), $G_{HP}E$ (green), and GE (magenta) mice. (I) (i) Histograms of ISI for layer 2/3 prefrontal neurons during ramp stimulation of hippocampal CA1 pyramidal neurons for CON (black), $G_{HP}E$ (green), and GE (magenta) mice. Note the prominent ISI peak at ∼16.7 Hz. (ii) Line plots of frequency-dependent relative power of hippocampal spike-triggered LFP in prefrontal layer 2/3 of CON (black), $G_{HP}E$ (green), and GE (magenta) mice. (J)

12–18 Hz), yet it did not induce a coherence increase in mice with whole-brain DISC1 suppression (Table 1, Fig. 3J). Even when the DISC1 suppression is confined to HP, the coherence did not significantly increase during ramp stimulus and augmented mainly after it, most likely as result of nonspecific network boosting.

Besides the reduced efficient activation of CA1 pyramidal neurons, abnormal connectivity might lead to dysfunction within prefrontal–hippocampal circuits in neonatal $G_{HP}E$ and GE mice. To test this hypothesis, we examined the evoked response in PFC by pulsed light stimulation of HP (see Supplementary Fig. 1B). In line with the larger density of hippocampal projections targeting prelimbic layer 5/6 than layer 2/3 neurons (Parent et al. 2010; Padilla-Coreano et al. 2016), the evoked response in layer 5/6 was stronger than in the layer 2/3 (see Supplementary Fig. 1Bi). Pulsed light stimulation in HP ensured that the activation of hippocampal neurons was timed. The delay of evoked responses in prelimbic layer 2/3 was significantly longer in $G_{HP}E$ (24.20 ± 0.79 ms, P = 0.0029) and GE (27.11 ± 1.65 ms, P = 0.0008) mice compared with CON (20.41 ± 0.18 ms, $F_{(2, 38)}$ = 5.37, P = 0.008, one-way ANOVA) mice (see Supplementary Fig. 1Bii). This result suggests that the connectivity between PFC and HP in $G_{HP}E$ and GE mice is impaired. Of note, no significant differences of the delay were observed for evoked responses in layer 5/6 of PFC in all three groups (see Supplementary Fig. 1Biii).

Taken together, these results indicate that hippocampal DISC1 suppression in combination with MIA lead to CA1 dysfunction that, on its turn, causes abnormal coupling within neonatal prefrontal–hippocampal networks.

DISC1 Knock-Down Causes Major Morphological and Synaptic Deficits of Pyramidal Neurons in CA1 Area

The abnormal firing and oscillatory entrainment of HP and consequently, the weaker prelimbic-hippocampal coupling in GE and $G_{HP}E$ mice might relate to abnormal morphology and connectivity of CA1 pyramidal neurons. To test this hypothesis, we undertook a detailed histological examination of the cytoarchitecture of tDimer-labeled hippocampal pyramidal neurons of P10 CON, $G_{HP}E$ and GE mice (n = 17–19 neurons from three mice in each group). The complexity of dendritic branching was assessed by Sholl analysis of three-dimensionally reconstructed hippocampal pyramidal neurons. When compared with CON mice, both $G_{HP}E$ and GE mice showed a highly significant reduction of dendritic branching of hippocampal pyramidal neurons (condition effect, $P < 1 \times 10^{-9}$) (Fig. 4A). These deficits were particularly prominent within a radius of 20–150 µm from the cell soma center. Next, we examined the spine density along the dendrites of hippocampal pyramidal neurons. In $G_{HP}E$ and GE mice, the density of dendritic spines was significantly lower when compared with CON mice (Fig. 4B,C). The magnitude of reduction was similar for basal dendrites ($F_{(2, 49)}$ = 10.21, P = 1.96 × 10^{-4}, one-way ANOVA), proximal oblique dendrites ($F_{(2, 50)}$ = 9.31, P = 3.66 × 10^{-4}, one-way ANOVA), and secondary apical dendrites ($F_{(2, 48)}$ = 8.14, P = 9.03 × 10^{-4}, one-way ANOVA). Thus, CA1 pyramidal neurons in $G_{HP}E$ and GE mice show simplified dendritic arborization and decreased spine density. As a

consequence, the hippocampal activity, especially the excitability of individual neurons and the locally generated SPWs, might be perturbed and the coupling with downstream prelimbic neurons, diminished.

Hippocampal DISC1 Knock-Down in Immune-Challenged Mice Causes Neuronal and Network Deficits as well as Cognitive Impairment at Prejuvenile Age

To test the long-term consequences of hippocampal dysfunction and abnormal prefrontal–hippocampal coupling, we investigated CON, GE, and $G_{HP}E$ mice at prejuvenile age (P20–P23) (Fig. 5A).

The DISC1 suppression persisted, yet at a lower magnitude, until this age, as revealed by the significantly ($F_{(1,146)}$ = 25.323, P = 4.85*10^{-7}, one-way ANOVA) lower DISC1 expression in $G_{HP}E$ (n = 73 neurons) when compared with CON (n = 75 neurons) mice (Fig. 5B). Of note, CA1 pyramidal neurons seem to respond to IUE shRNA suppression differently compared with prelimbic neurons, where the DISC1 knock-down was temporally restricted to the neonatal period (Xu et al. 2019).

First, we performed multisite extracellular recordings of LFP from PL and hippocampal CA1 area of urethane-anesthetized P20–23 CON (n = 12), $G_{HP}E$ (n = 9), and GE (n = 15) mice. All investigated mice showed continuous large-amplitude slow rhythms that were superimposed with oscillatory activity in theta (4–12 Hz) and gamma (30–100 Hz) frequencies. These patterns of network activity correspond to the sleep-like rhythms mimicked by urethane anesthesia (Wolansky et al. 2006; Clement et al. 2008). While the impairment of neuronal firing, SPW, and network oscillations was less pronounced at prejuvenile age when compared with the deficits at neonatal age, the directed interactions between PFC and HP were still compromised (Fig. 5C). Both GE (0.123 ± 0.003, P = 0.016, ANOVA followed by Bonferroni-corrected post hoc test) and $G_{HP}E$ (0.127 ± 0.004, P = 0.002, ANOVA followed by Bonferroni-corrected post hoc test) mice had smaller gPDC peaks within theta band (4–8 Hz) and thus, weaker drive from HP to PFC, when compared with CON mice (0.147 ± 0.007) mice. Light stimulation of ChR2(ET/TC)-expressing CA1 neurons augmented the power of network oscillations in theta-beta range for CON (theta: 0.404 ± 0.096; beta: 0.283 ± 0.061), but not GE and $G_{HP}E$ mice (Fig. 5Di). Mirroring the weaker hippocampal drive, the light stimulation of HP augmented the power of prefrontal oscillations in theta (0.373 ± 0.094) and beta (0.269 ± 0.052) range only in CON, whereas the increase was smaller, if any, for GE (4–12 Hz: 0.061 ± 0.0750, P = 0.0009; 12–30 Hz: 0.0640 ± 0.048, P = 0.0009, one-way ANOVA followed by Bonferroni-corrected post hoc test) and $G_{HP}E$ (4–12 Hz: 0.160 ± 0.044, P = 0.007; 12–30 Hz: 0.144 ± 0.040, P = 0.003, one-way ANOVA followed by Bonferroni-corrected post hoc test) mice (Fig. 5Dii). Similar to neonatal age, these functional deficits were related to abnormal morphology and connectivity of CA1 neurons. Detailed histological examination of the cytoarchitecture revealed that at P20 the dendritic branching of hippocampal pyramidal neurons in GE and $G_{HP}E$ mice was still significantly reduced when compared with CON (n = 17–19 neurons from three mice in each group)

Line plots of coherence between PFC and HP during ramp stimulation of hippocampal CA1 pyramidal neurons normalized to coherence values before stimulation. Single data points are represented as dots and the red horizontal bars in violin plots correspond to the median and the 25th and 75th percentiles. *$P < 0.05$, **$P < 0.01$, ***$P < 0.001$. Magenta stars correspond to the comparison between GE and CON mice. Green stars correspond to the comparison between $G_{HP}E$ and CON mice.
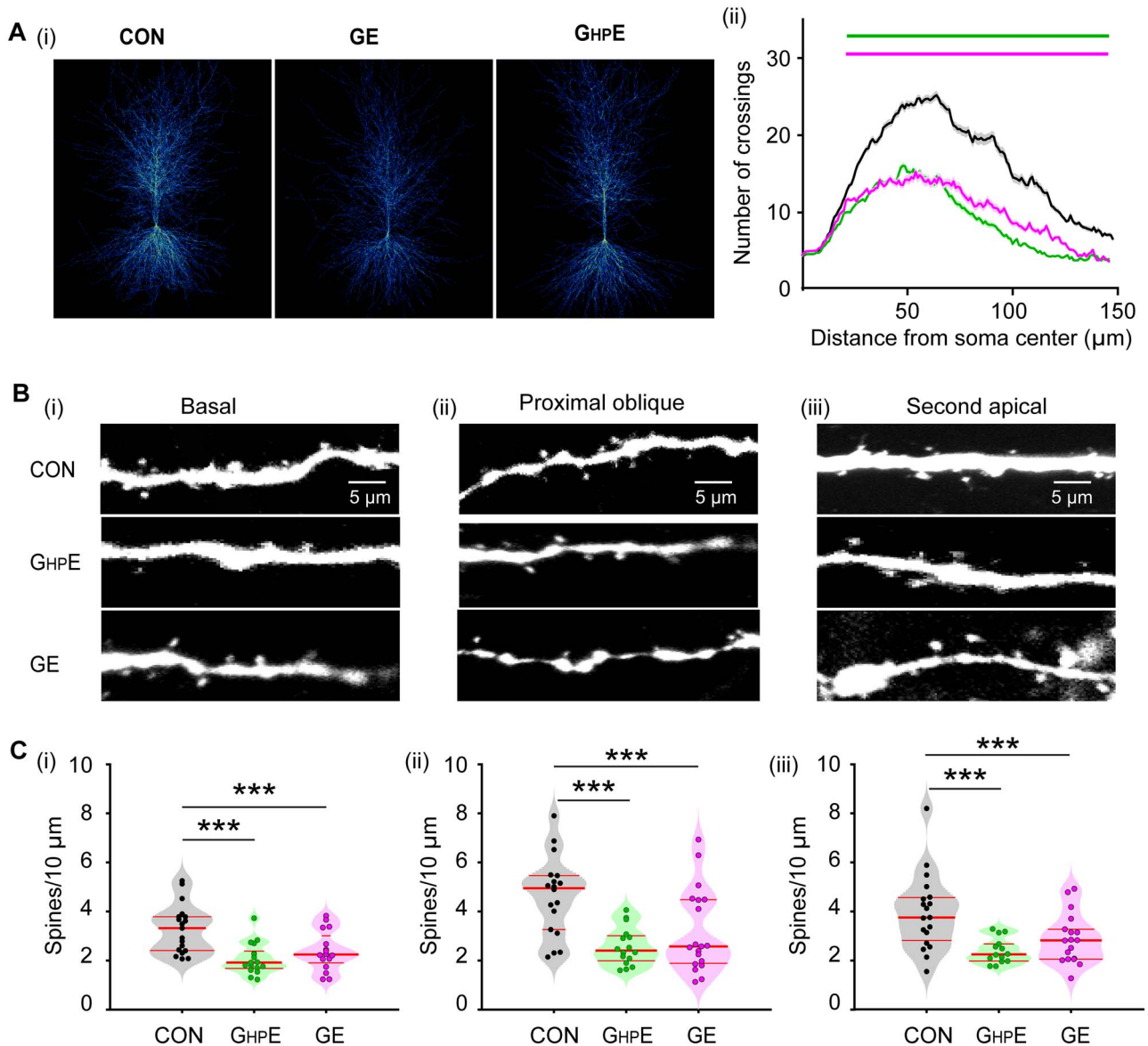
Figure 4. Morphology of hippocampal pyramidal neurons in neonatal $G_{HP}E$ and GE mice. (A) (i) Heatmap displaying an overlay of all traced dendrites of transfected CA1 pyramidal neurons in CON, $G_{HP}E$, and GE mice. (ii) Graph displaying the average number of dendritic intersections within a 150 μm radius from the soma center of CA1 pyramidal neurons in CON (black, $n = 21$ neurons from three mice), $G_{HP}E$ (blue, $n = 21$ neurons from three mice) and GE (red, $n = 21$ neurons from three mice) mice. Green and magenta bars indicate significant difference (***$P < 0.001$) between CON and $G_{HP}E$ mice and between CON and GE mice, respectively. (B) Photograph displaying representative basal (i), proximal oblique (ii) and second apical dendrites (iii) of CA1 pyramidal neurons from a P9 CON, a P9 $G_{HP}E$, and a P9 GE mouse. (C) Violin plots displaying the spine density on basal (i), proximal oblique (ii), and second apical dendrites (iii) of CA1 pyramidal neurons from CON (20 neurons from three mice), $G_{HP}E$ (20 neurons from three mice), and GE (21 neurons from three mice) mice. Single data points are represented as dots and the red horizontal bars in violin plots correspond to the median and the 25th and 75th percentiles. ***$P < 0.001$.

mice (condition effect, $P = 7.30 \times 10^{-9}$) (Fig. 5E). These deficits were particularly prominent within a radius of 40–150 μm from the cell soma center. The sparsification of dendritic projections was accompanied by lower density of the dendritic spines in $G_{HP}E$ and GE mice when compared with CON mice (Fig. 5F). The magnitude of density reduction was similar for basal dendrites ($F(2, 52) = 46.36$, $P = 2.77 \times 10^{-12}$, one-way ANOVA), proximal oblique dendrites ($F(2, 54) = 31.81$, $P = 7.44 \times 10^{-10}$, one-way ANOVA), and secondary apical dendrites ($F(2, 53) = 20.22$, $P = 2.97 \times 10^{-7}$, one-way ANOVA).

Taken together, these data show that the prefrontal–hippocampal dysfunction resulting from synaptic and projection deficits of CA1 pyramidal neurons in GE and $G_{HP}E$ mice persists until prejuvenile age.

The developmental prefrontal–hippocampal dysfunction as result of hippocampal DISC1 suppression in immune-challenged mice might cause behavioral disabilities. Already at juvenile age, rodents have reliable novelty detection and recognition memory that rely on the mouse's intrinsic exploratory drive and require no prior training or deprivation (Kruger
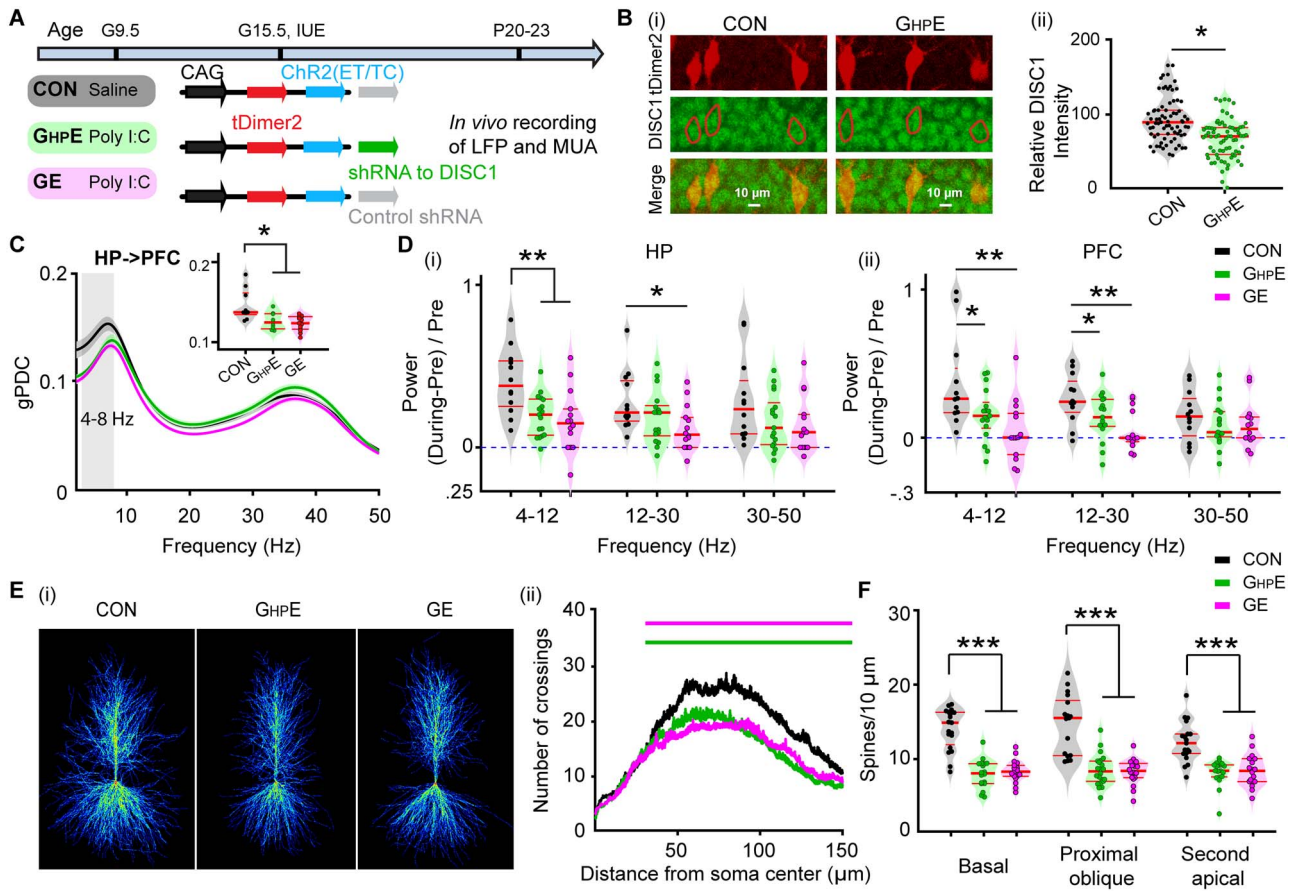
Figure 5. Patterns of prejuvenile network and neuronal firing in the CA1 area of i/vHP of immune challenged mice with whole-brain or HP-confined DISC1 suppression. (A) Timeline of experimental protocol and description of the three investigated groups of mice: CON, G$_{HP}$E, and GE. For each group the constructs used for IUE to target hippocampal CA1 pyramidal neurons is specified. (B) (i) Photographs displaying the DISC1 immunoreactivity (green) in relationship with the tDimer2-expression (red) in the CA1 area of i/vHP of P21 G$_{HP}$E and CON mice. (ii) Violin plots displaying the relative DISC1 immunoreactivity averaged for G$_{HP}$E and CON mice at P20–P23. (C) Line plots of mean gPDC in relationship to frequency for HP→PFC in CON (black), G$_{HP}$E (green) and GE (magenta) mice. Inset, violin plots displaying gPDC when averaged for 4–8 Hz in CON, G$_{HP}$E, and GE mice. (D) Violin plots displaying the hippocampal (i) and prefrontal (ii) oscillatory power averaged for different frequency bands (4–12 Hz, 12–30 Hz, 30–50 Hz) in response to ramp stimulation in HP for all investigated mice. (E) (i) Heatmap displaying an overlay of all traced dendrites of transfected CA1 pyramidal neurons in CON, G$_{HP}$E, and GE mice. (ii) Graph displaying the average number of dendritic intersections within a 150 μm radius from the soma center of CA1 pyramidal neurons in CON (black, $n = 21$ neurons from three mice), G$_{HP}$E (blue, $n = 21$ neurons from three mice) and GE (red, $n = 21$ neurons from three mice) mice. Green and magenta bars indicate significant difference (***$P < 0.001$) between CON and G$_{HP}$E mice and between CON and GE mice, respectively. (F) Violin plots displaying the spine density on basal, proximal oblique, and second apical dendrites of CA1 pyramidal neurons from CON, G$_{HP}$E, and GE mice. Single data points are represented as dots and the red horizontal bars in violin plots correspond to the median and the 25th and 75th percentiles. *$P < 0.05$, **$P < 0.01$, ***$P < 0.001$.

et al. 2012). These abilities have been shown to involve communication within a circuit centered on PFC and HP (Warburton and Brown 2015). Both GE mice and immune-challenged mice with DISC1 suppression confined to PFC have been reported to have poor recognition memory (Hartung et al. 2016; Xu et al. 2019). To identify the consequences of perinatal HP-restricted DISC1 knock-down on cognitive abilities, we tested NOR and RR in CON ($n = 11$), G$_{HP}$E ($n = 13$), and GE ($n = 12$) mice using a custom-designed arena (Fig. 6A) and previously established protocols (Fig. 6Bi and Ci). During the familiarization trials of these tests, all mice spent equal time investigating the two objects placed in the arena. During the NOR test trial protocols, CON mice spent significantly ($P = 2.38 \times 10^{-5}$, paired t-test) longer time interacting with the novel object (79.12 ± 4.49%) than with the familiar one (20.88 ± 4.49%) (Fig. 6Bii). In line with previous results, GE mice did not show a preference for the novel object (familiar: 47.46 ± 7.90%; novel: 52.54 ± 7.90%, $P = 0.372$, paired t-test) (Fig. 6Bii). Similarly, prejuvenile G$_{HP}$E

mice also did not show a preference for the novel object during test trial (familiar: 39.23 ± 1.29%; novel: 60.77 ± 2.19%, $P = 0.07$, paired t-test) (Fig. 6Bii). Correspondingly, the discrimination ratio between the familiar and the novel object significantly decreased in GE (0.0501 ± 0.158, $P = 0.02$, one-way ANOVA followed by Bonferroni-corrected post hoc test) and G$_{HP}$E mice (−0.215 ± 0.142, $P = 0.02$, one-way ANOVA followed by Bonferroni-corrected post hoc test) compared with CON mice (0.582 ± 0.090) (Fig. 6Biii).

During RR task, mice process temporal information by recognizing the object with which they most recently interacted. The CON mice spent more time with the object they explored during the first familiarization trial and less time with the more recent object from the second familiarization trial (old: 67.52 ± 4.72%, recent: 32.48 ± 4.72%, $P = 0.0015$, paired t-test) (Fig. 6Cii). Both G$_{HP}$E and GE mice did not show a preference for the object in the first familiarization trial and spent equal time with both objects (GE, old: 50.88 ± 3.92%, recent: 49.12 ± 3.92%, $P = 0.409$, paired
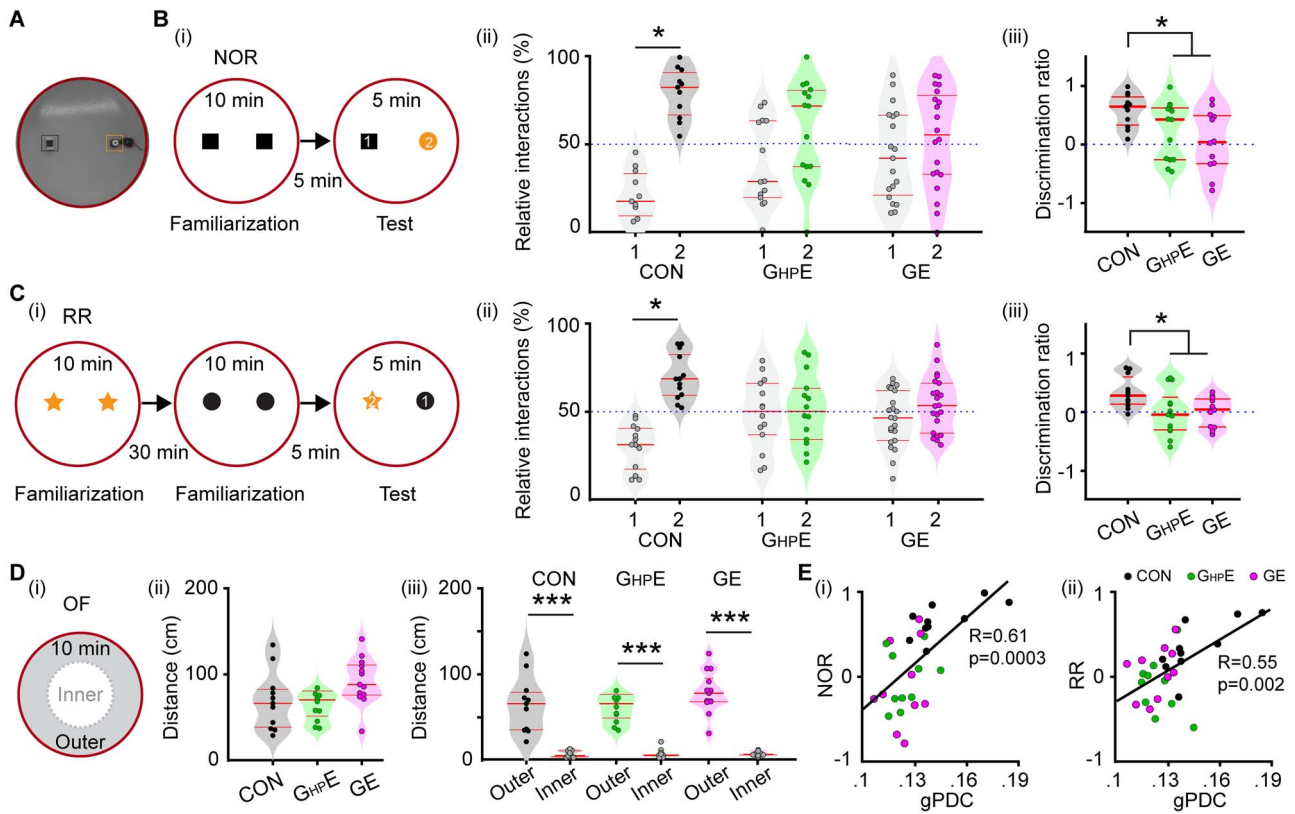
Figure 6. Novelty recognition of immune challenged mice with whole-brain and HP-confined DISC1 suppression. (A) Photograph of the arena used for NOR and RR tasks. (B) (i) Schematic diagrams of the protocol for NOR task. (ii) Violin plots displaying the relative interaction time spent by CON, $G_{HP}E$, and GE mice with the objects during the NOR test trial. The dotted line indicates chance level. (iii) Violin plots displaying the NOR discrimination ratio when averaged for CON, $G_{HP}E$ and GE mice. (C) (i) Schematic diagrams of the protocol for RR task. (ii) Violin plots displaying the relative interaction time spent by CON, $G_{HP}E$, and GE mice with the objects during the RR test trial. The dotted line indicates chance level. (iii) Violin plots displaying the RR discrimination ratio when averaged for CON, $G_{HP}E$, and GE mice. (D) (i) Schematic diagrams of the protocol for OF task. (ii) Violin plots displaying the distance covered in 10 min by CON, $G_{HP}E$, and GE mice during the OF task. (iii) Violin plots displaying the distance covered in the outer circle and the inner circle by CON, $G_{HP}E$, and GE mice during OF task. (E) (i) The Pearson's correlation between gPDC and discrimination ratio in NOR task. (ii) Same as (i) for Pearson's correlation between gPDC and RR. Single data points are represented as dots and the red horizontal bars in violin plots represent the median and the 25th and 75th percentiles. *$P < 0.05$, ***$P < 0.001$.

t-test; $G_{HP}E$, old: $50.86 \pm 5.93\%$, recent: $49.14 \pm 5.93\%$, $P = 0.441$, paired t-test) (Fig. 6Cii). Correspondingly, the discrimination ratio significantly decreased in GE (0.001 ± 0.075, $P = 0.04$, one-way ANOVA followed by Bonferroni-corrected post hoc test) and $G_{HP}E$ (-0.0053 ± 0.1133, $P = 0.03$, one-way ANOVA followed by Bonferroni-corrected post hoc test) compared with the values for CON mice (0.335 ± 0.087) (Fig. 6Ciii).

The poor performance in NOR and RR tasks may result from poor motor abilities and/or enhanced anxiety when interacting with the objects. To test this hypothesis, we analyzed the exploratory behavior of P16 mice from all three groups during OF task (Fig. 6Di). The distance covered in 10 min was similar in all groups (CON: 69.176 ± 10.70 cm; GE: 77.41 ± 12.11 cm; $G_{HP}E$: 92.25 ± 7.86 cm, $F(2, 33) = 1.437$, $P = 0.252$, one-way ANOVA) (Fig. 6Dii). Moreover, the distance covered in the outer circle was much larger than in the inner circle of the arena (CON: 64.67 ± 10.18 cm vs. 4.50 ± 1.18 cm; GE: 72.62 ± 10.81 cm vs. 4.78 ± 1.51 cm; $G_{HP}E$: 79.23 ± 7.00 cm vs. 5.02 ± 0.73 cm) (Fig. 6Diii). During the sample trial of NOR task, mice from all groups covered a similar distance as well (see Supplementary Fig. 2). These results indicate that exploratory and anxiety

abilities were similar in CON, $G_{HP}E$, and GE mice and thus, did not affect the recognition memory in NOR and RR tasks.

To better link the behavioral deficits in GE and $G_{HP}E$ mice with the abnormal prefrontal–hippocampal coupling, we performed the Pearson's correlation between gPDC and discrimination ratio in NOR and RR task (Fig. 6E). There was strong positive correlation between gPDC and NOR ($R = 0.61$, $P = 0.0003$, Pearson's correlation) and between gPDC and RR ($R = 0.55$, $P = 0.002$, Pearson's correlation). Given the prior group differences, a generalized linear model (GLM) with group comparisons was used to predict the animals' behavioral performance in NOR and RR tasks by the factor of prefrontal–hippocampal coupling measured with gPDC. Group comparisons were performed with GLM by including the factor of group as predictor variable. Significant positive correlation was found in gPDC-NOR ($R = 11.23$, $P = 0.027$) with significant group effect ($P = 0.014$). There was also a significant positive correlation in gPDC-RR ($R = 11.14$, $P = 0.011$), yet without significant group effect ($P = 0.75$). These results confirmed that abnormal prefrontal–hippocampal coupling as results of HP-restricted DISC1 suppression in immune challenged mice correlates to the poorer recognition memory at prejuvenile age.

Table 1 Prefrontal–hippocampal activity patterns and coupling in CON, $G_{HP}E$, and GE mice

		CON	$G_{HP}E$	GE	F value
HP					
Spindle bursts	Occurrence (per min)	8.73 ± 0.31	9.52 ± 0.29	9.47 ± 0.38	F(2,53) = 1.94 P = 0.15
	Duration (s)	4.46 ± 0.24	3.67 ± 0.15 *P = 0.021	3.38 ± 0.18 **P = 0.0005	F(2,53) = 8.72 P = 0.0005
	Power (4–50 Hz)	30.63 ± 4.93	12.37 ± 1.72 *P = 0.034	18.23 ± 3.32 *P = 0.05	F(2,53) = 5.87 P = 0.005
SPWs	Occurrence (Hz)	0.41 ± 0.02	0.37 ± 0.02 *P = 0.034	0.36 ± 0.02 *P = 0.024	F(2,52) = 2.73 P = 0.05
	SWP-Spike	0.76 ± 0.08	0.40 ± 0.11 *P = 0.019	0.47 ± 0.09 *P = 0.05	F(2,51) = 4.74 P = 0.013
PL					
Spindle bursts	Occurrence (per min)	7.88 ± 0.33	8.87 ± 0.26	8.07 ± 0.39	F(2,47) = 2.60 P = 0.09
	Duration (s)	3.05 ± 0.17	2.47 ± 0.13 *P = 0.030	2.41 ± 0.17 *P = 0.021	F(2,47) = 5.29 P = 0.008
	Power (4–50 Hz)	10.12 ± 1.31	6.41 ± 0.60 *P = 0.049	6.33 ± 0.94 *P = 0.029	F(2,53) = 4.49 P = 0.016
MUA	Layer2/3 (log)	−0.71 ± 0.16	−0.45 ± 0.21	−1.96 ± 0.24 *P = 0.030	F(2,39) = 3.55 P = 0.038
	Layer5/6 (log)	−3.06 ± 0.30	−2.18 ± 0.35	−3.36 ± 0.61	F(2,39) = 2.35 P = 0.108
HP-PL	PLV (4–30 Hz)	0.19 ± 0.01	0.15 ± 0.02 *P = 0.037	0.15 ± 0.01 *P = 0.049	F(2,51) = 4.20 P = 0.021
	gPDC (4–30 Hz)	0.068 ± 0.004	0.050 ± 0.004 *P = 0.014	0.053 ± 0.005 *P = 0.036	F(2,53) = 5.26 P = 0.008

Data are shown as mean ± SEM. Significance was assessed using one-way ANOVA test followed by Bonferroni-corrected post hoc test and the listed P values correspond to comparisons between CON and $G_{HP}E$ mice, CON and GE mice. *P < 0.05, **P < 0.01.

Table 2 Prefrontal–hippocampal activity patterns and coupling induced by activating CA1

		CON	$G_{HP}E$	GE	F values
Activating HP by pulses stimulation					
PFC Power (During-pre)/pre	4–12 Hz	0.234 ± 0.049	0.059 ± 0.042 *P = 0.016	0.023 ± 0.047 **P = 0.005	F(2,45) = 6.47 P = 0.0034
	12–30 Hz	0.210 ± 0.049	0.045 ± 0.032 **P = 0.0096	−0.007 ± 0.039 **P = 0.0011	F(2,45) = 8.21 P = 0.0009
	30–45 Hz	0.184 ± 0.035	0.051 ± 0.027 **P = 0.007	0.004 ± 0.030 ***P = 0.0004	F(2,45) = 9.38 P = 0.0004
Activating HP by ramp stimulation					
HP Power (During-pre)/pre	4–12 Hz	0.186 ± 0.045	0.070 ± 0.031 *P = 0.011	0.026 ± 0.050 *P = 0.024	F(2,45) = 3.98 P = 0.026
	12–30 Hz	0.267 ± 0.051	0.091 ± 0.043 *P = 0.018	0.046 ± 0.043 **P = 0.004	F(2,45) = 6.62 P = 0.003
	30–45 Hz	0.224 ± 0.054	0.102 ± 0.046	0.089 ± 0.049	F(2,45) = 2.34 P = 0.108
Spike-triggered LFP	15–40 Hz	3.08 ± 0.59	1.43 ± 0.27 *P = 0.018	1.42 ± 0.40 *P = 0.021	F(2,43) = 5.26 P = 0.009
PFC2/3 Firing interval		0.020 ± 0.001	0.015 ± 0.002 *P = 0.04	0.014 ± 0.002 **P = 0.005	F(2,39) = 6.37 P = 0.004
HP spike-triggered LFP	15–40 Hz	7.06 ± 2.19	3.03 ± 0.72 *P = 0.044	2.90 ± 0.88 *P = 0.042	F(2,45) = 3.22 P = 0.049
PFC-HP Coherence	12–18 Hz	0.220 ± 0.044	0.041 ± 0.023 ***P = 0.0003	−0.004 ± 0.024 ***P = 0.00001	F(2,41) = 15.33 P = 0.000001

Data are shown as mean ± SEM. Significance was assessed using one-way ANOVA test followed by Bonferroni-corrected post hoc test and the listed P values correspond to comparisons between CON and $G_{HP}E$ mice, CON and GE mice. *P < 0.05, **P < 0.01, ***P < 0.001.

Discussion

Developmental miswiring of the brain has been hypothesized to account for cognitive impairment in mental disorders. Previous studies provided first experimental evidence that the communication between PFC and HP, the core of a complex network underlying mnemonic and executive processing, is substantial impaired in mouse models of disease already at neonatal age (Hartung et al. 2016; Oberlander et al. 2019). The mechanisms causing diminished communication within prefrontal–hippocampal networks during development remain largely unknown. We recently identified spine loss and sparsification of dendritic projections in layer 2/3 pyramidal neurons of neonatal PFC as one mechanism of disorganized network activity and reduced coupling with HP (Xu et al. 2019; Chini et al. 2020). These findings were consistent with the previous data from adult mice, which demonstrated that specific prefrontal DISC1 knock-down induced abnormal neuronal development and cognitive behaviors (Niwa et al. 2010; Saito et al. 2016). It is still unclear whether hippocampal dysfunction contributes to the early miswiring as well. Here, we combine electrophysiology and optogenetics in vivo with neuroanatomy and behavioral testing of immune challenged mice with either brain-wide or HP-confined suppression of DISC1. We provide evidence that (i) highly fragmented oscillatory activity with reduced power, fewer SPWs and decreased SPW-related firing of CA1 neurons in the i/vHP are present in both GE and G$_{HP}$E mice; (ii) confinement of DISC1 knock-down to HP of immune challenged mice causes weaker hippocampal drive to PFC and consequently, abnormal prefrontal network activity, despite nonaffected firing rates over cortical layers; (iii) HP-confined or brain-wide DISC1 suppression similarly impairs the morphology of CA1 neurons, reducing the dendritic branching and the density of spines; (iv) the morphological and functional deficits in the HP of GE and G$_{HP}$E mice persist until prejuvenile age leading to cognitive impairment and long-lasting disruption of underlying prefrontal–hippocampal communication.

The severe morphological and functional impairment of the developing HP when DISC1 is suppressed goes in line with previous studies that identified this gene as a hub of maturational processes (Miyoshi et al. 2003; Duan et al. 2007). Especially DISC1 knock-down in HP has been associated with long-lasting deficits and behavioral impairment related to mental disorders (Callicott et al. 2005; Meyer and Morris 2008). DISC1 controls neurite growth, neuronal migration, and differentiation as well as axon targeting (Niwa et al. 2010; Narayan *et al.* 2013; Saito et al. 2016). In line with this function, the hippocampal structure and neuronal distribution across layers in the i/vHP was disturbed in GE mice when compared with controls. This result was consistent with the previous report by Tomita et al. (2011), which showed that knockdown of DISC1 in the HP of developing mouse resulted in impaired migration of dorsal CA1 pyramidal neurons. Intriguingly, it was also reported that HP-confined DISC1 suppression did not perturb the migration of CA1 pyramidal neurons in the dorsal HP but hindered the migration of dentate gyrus granule cells (Meyer and Morris 2009). The arborization and synaptic interactions of CA1 pyramidal neurons seem to be profoundly altered. The sparsification of their dendritic branching and the low number of spines document major developmental deficits of CA1 neurons when DISC1 was locally suppressed. These might result from disorganized microtubule-associated dynein motor complex (Ozeki et al. 2003; Kamiya et al. 2005). Moreover, lower density of axonal projections might link HP to PFC, as

previously observed from GE mice. The abnormal morphology is likely to underlie the early dysfunction of activity patterns generated within CA1 (e.g., SPWs, beta–gamma oscillations) and the diminishment of excitatory drive to PFC.

Suppression of DISC1 decreased the occurrence of SPWs and the SPW-related neuronal firing. While SPWs have been extensively characterized in the adult HP (Buzsaki 1986), their underlying mechanisms during development are still largely unknown. SPWs emerge early in life (Nowack et al. 1989; Brockmann et al. 2011; Valeeva et al. 2019). Similar to adult one, the neonatal SPWs seem to be generated within HP following population bursts in CA3 area. They correlate with increased firing rate of hippocampal neurons. The decreased SPWs occurrence and related neuronal discharge indicate that DISC1 suppression might cause miswiring within HP and abnormal coupling between CA1 and CA3. Accordingly, both pulse and ramp stimuli induced hippocampal firing. However, the power of spike-triggered LFP in CA1 dramatically decreased in GE and G$_{HP}$E mice, reflecting a weaker entrainment of local circuits in HP triggered by neuronal firing. Correspondingly, the power of oscillations in beta and gamma frequency range decreased in GE and G$_{HP}$E mice as well. In contrast, the theta bursts were less affected, their occurrence being similar across all investigated mice. This might be due to the fact that theta bursts have a multiple mostly extra-hippocampal origin with the septum as one main generator (Janiesch et al. 2011). At adulthood, the SPW-ripple events were still perturbed in different strains with suppressed DISC1, yet their occurrence was higher when compared with controls due to dysfunction of parvalbumin-positive interneurons (Altimus et al. 2015). We propose that the abnormal maturation of hippocampal circuits might have detrimental effects on the interneuron function and cause overcompensation resulting in hippocampal hyperexcitability.

Several lines of evidence show that DISC1 suppression perturbs not only the hippocampal activity and oscillatory entrainment but also the prefrontal activity and the communication within prefrontal–hippocampal networks. First, even when confined to HP, DISC1 suppression led to disorganized prefrontal activity with weaker power. In contrast, the overall firing of neurons in the PL remained unaffected. In contrast, when the DISC1 suppression was restricted to PFC, the firing of these neurons was dramatically decreased (Xu et al. 2019). Second, the timing of prelimbic firing in G$_{HP}$E mice was disturbed by the HP-confined DISC1 suppression, the characteristic beta band peak of firing interval and HP-spike triggered LFP power in layer 2/3 of PFC being absent in these mice. Third, the synchrony over a wide frequency range and the directionality of prefrontal–hippocampal interactions diminished in GE and G$_{HP}$E mice when compared with controls. Moreover, during ramp light stimulation the coherence of prefrontal–hippocampal interactions within beta-frequency range was significantly decreased in both GE and G$_{HP}$E mice, reflecting the weaker excitatory drive from the HP to PFC.

We propose that two mechanisms contribute to the abnormal prefrontal–hippocampal communication of GE and G$_{HP}$E. On the one hand, due to synaptic deficits and the sparsification of dendritic branching, the CA1 pyramidal neurons lose to a large extent the ability to fire in an oscillatory phase-coordinated manner. Consequently, the excitatory drive reaching mainly layer 5/6 of PFC (Parent et al. 2010; Padilla-Coreano et al. 2016) decreases and the boosting of intracortical connectivity resulting in beta entrainment within layer 2/3 is weaker. On the other hand, the sparsification of axonal projections might cause less

dense connections to the PFC. Whether the glutamate release of the hippocampal terminals targeting the PFC is also impaired remains to be elucidated.

In contrast to the DISC1 suppression confined to the pyramidal neurons in PFC, the DISC1 suppression in HP is not transient during development but persisted until prejuvenile age. These differences across areas might result from different regulation of Disc1 gene by external cues. Over 50 proteins interact with DISCI controlling different maturational processes (Camargo et al. 2007; Ye et al. 2017). Despite similar DISC1 knock-down by shRNA, these interactions may lead to major differences across brain regions and over time. The interference of DISC1 with immune-relevant signaling pathways is of particular relevance (Beurel et al. 2010). The structural and functional deficits caused by the combination of DISC1 suppression with MIA are by far more pronounced than the effects induced by either of the two factors. They persist throughout the life span, leading to altered social and cognitive behavior (Abazyan et al. 2010; Ibi et al. 2010; Lipina et al. 2013). In the present study, we identified morphological and functional deficits within prefrontal–hippocampal networks of $G_{HP}E$ mice until prejuvenile age. This abnormal communication between the two brain areas throughout the development relates to impaired prejuvenile cognitive performance, which requires the prefrontal–hippocampal activation (Barker and Warburton 2011). The ability to recognize new objects and their recency was absent in GE and $G_{HP}E$ mice.

While comprehensive genome-wide association studies showed that DISC1 is unlikely to be a "genetic" factor causing schizophrenia (Schizophrenia Working Group of the Psychiatric Genomics Consortium 2014; Sullivan et al. 2012; Ripke et al. 2013), a wealth of data documented its relevance for psychiatric conditions (Tomoda et al. 2016, 2017; Trossbach et al. 2016; Kakuda et al. 2019; Sawa 2019). Orchestrating molecular cascades hypothesized to underlie disease-relevant physiological and behavioral abnormalities (Cuthbert and Insel 2013). DISC1 points out the contribution of abnormal development for multiple mental conditions. The present results provide first insight into the mechanisms by which DISC1 suppression interferes with the circuit function and cognitive abilities. They show that besides prefrontal deficits of layer 2/3 pyramidal neurons, the dysfunction of hippocampal CA1 neurons unable to drive the down-stream PFC during early development causes impaired prefrontal–hippocampal communication that relates to poor cognitive performance. HP plays a key role for memory deficits in mental disorders (Chen et al. 2018). Impairment of hippocampal recruitment during memory tasks has been described for schizophrenia patients and high-risks subjects (Di Giorgio et al. 2013; Rasetti et al. 2014). We provide experimental evidence that developmental miswiring in HP might cause cognitive deficits at adulthood and disrupt the prefrontal–hippocampal coupling. Weaker coactivation of PFC and HP has been identified in schizophrenia patients during cognitive tasks (Meyer-Lindenberg et al. 2001). Thus, the present study supports the neurodevelopmental origin of schizophrenia and highlights the hub function of HP during early maturation for the functional and cognitive deficits at adulthood.

Supplementary Material

Supplementary material can be found at *Cerebral Cortex* online.

Notes

References

Abazyan B, Nomura J, Kannan G, Ishizuka K, Tamashiro KL, Nucifora F, Pogorelov V, Ladenheim B, Yang C, Krasnova IN, et al. 2010. Prenatal interaction of mutant DISC1 and immune activation produces adult psychopathology. *Biol Psychiatry*. 68:1172–1181.

Ahlbeck J, Song L, Chini M, Bitzenhofer SH, Hanganu-Opatz IL. 2018. Glutamatergic drive along the septo-temporal axis of hippocampus boosts prelimbic oscillations in the neonatal mouse. *Elife*. 7:e33158.

Altimus C, Harrold J, Jaaro-Peled H, Sawa A, Foster DJ. 2015. Disordered ripples are a common feature of genetically distinct mouse models relevant to schizophrenia. *Mol Neuropsychiatry*. 1:52–59.

Baccala LA, Sameshima K. 2001. Partial directed coherence: a new concept in neural structure determination. *Biol Cybern*. 84:463–474.

Baccala LA, Sameshima K, Takahashi DY. 2007. *Generalized partial directed coherence. In: 2007 15th International Conference on Digital Signal Processing*: 163–166.

Backus AR, Schoffelen JM, Szebenyi S, Hanslmayr S, Doeller CF. 2016. Hippocampal-prefrontal theta oscillations support memory integration. *Curr Biol*. 26:450–457.

Barker GR, Warburton EC. 2011. When is the hippocampus involved in recognition memory? *J Neurosci*. 31:10721–10731.

Baumgart J, Grebe N. 2015. C57BL/6-specific conditions for efficient in utero electroporation of the central nervous system. *J Neurosci Methods*. 240:116–124.

Berndt A, Schoenenberger P, Mattis J, Tye KM, Deisseroth K, Hegemann P, Oertner TG. 2011. High-efficiency channelrhodopsins for fast neuronal stimulation at low light levels. *PNAS*. 108:7595–7600.

Beurel E, Michalek SM, Jope RS. 2010. Innate and adaptive immune responses regulated by glycogen synthase kinase-3 (GSK3). *Trends Immunol*. 31:24–31.

Bitzenhofer SH, Hanganu-Opatz IL. 2014. Oscillatory coupling within neonatal prefrontal-hippocampal networks is independent of selective removal of GABAergic neurons in the hippocampus. *Neuropharmacology*. 77:57–67.

Bitzenhofer SH, Ahlbeck J, Hanganu-Opatz IL. 2017a. Methodological approach for optogenetic manipulation of neonatal neuronal networks. *Front Cell Neurosci*. 11:239.

Bitzenhofer SH, Ahlbeck J, Wolff A, Wiegert JS, Gee CE, Oertner TG, Hanganu-Opatz IL. 2017b. Layer-specific optogenetic activation of pyramidal neurons causes beta-gamma entrainment of neonatal networks. *Nat Commun*. 8:14563.

Brockmann MD, Poschel B, Cichon N, Hanganu-Opatz IL. 2011. Coupled oscillations mediate directed interactions between prefrontal cortex and hippocampus of the neonatal rat. *Neuron*. 71:332–347.

Buzsaki G. 1986. Hippocampal sharp waves - their origin and significance. *Brain Res*. 398:242–252.

Buzsaki G. 2002. Theta oscillations in the hippocampus. *Neuron*. 33:325–340.

Cash-Padgett T, Jaaro-Peled H. 2013a. DISC1 mouse models as a tool to decipher gene-environment interactions in psychiatric disorders. *Front Behav Neurosci*. 7:113.

Callicott JH, Straub RE, Pezawas L, Egan MF, Mattay VS, Hariri AR, Verchinski BA, Meyer-Lindenberg A, Balkissoon R, Kolachana B, et al. 2005. Variation in DISC1 affects hippocampal structure and function and increases risk for schizophrenia. *PNAS*. 102:8627–8632.

Camargo LM, Collura V, Rain JC, Mizuguchi K, Hermjakob H, Kerrien S, Bonnert TP, Whiting PJ, Brandon NJ. 2007. Disrupted in schizophrenia 1 Interactome: evidence for the close connectivity of risk genes and a potential synaptic basis for schizophrenia. *Mol Psychiatry*. 12:74–86.

Cash-Padgett T, Jaaro-Peled H. 2013b. DISC1 mouse models as a tool to decipher gene-environment interactions in psychiatric disorders. *Front Behav Neurosci*. 7:113.

Chen LW, Sun D, Davis SL, Haswell CC, Dennis EL, Swanson CA, Whelan CD, Gutman B, Jahanshad N, Iglesias JE, et al. 2018. Smaller hippocampal CA1 subfield volume in posttraumatic stress disorder. *Depress Anxiety*. 35:1018–1029.

Chini M, Popplau JA, Lindemann C, Carol-Perdiguer L, Hnida M, Oberlander V, Xu X, Ahlbeck J, Bitzenhofer SH, Mulert C, et al. 2020. Resolving and rescuing developmental miswiring in a mouse model of cognitive impairment. *Neuron*. 105 e67:60–74.

Cichon NB, Denker M, Grun S, Hanganu-Opatz IL. 2014. Unsupervised classification of neocortical activity patterns in neonatal and pre-juvenile rodents. *Front Neural Circuits*. 8:50.

Clement EA, Richard A, Thwaites M, Ailon J, Peters S, Dickson CT. 2008. Cyclic and sleep-like spontaneous alternations of brain state under urethane anaesthesia. *PLoS One*. 3:e2004.

Crabtree GW, Sun Z, Kvajo M, Broek JA, Fenelon K, McKellar H, Xiao L, Xu B, Bahn S, O'Donnell JM, et al. 2017. Alteration of neuronal excitability and short-term synaptic plasticity in the prefrontal cortex of a mouse model of mental illness. *J Neurosci*. 37:4158–4180.

Cuthbert BN, Insel TR. 2013. Toward the future of psychiatric diagnosis: the seven pillars of RDoC. *BMC Med*. 11:126.

Di Giorgio A, Gelao B, Caforio G, Romano R, Andriola I, D'Ambrosio E, Papazacharias A, Elifani F, Bianco LL, Taurisano P, et al. 2013. Evidence that hippocampal-parahippocampal dysfunction is related to genetic risk for schizophrenia. *Psychol Med*. 43:1661–1671.

Duan X, Chang JH, Ge S, Faulkner RL, Kim JY, Kitabatake Y, Liu XB, Yang CH, Jordan JD, Ma DK, et al. 2007. Disrupted-in-schizophrenia 1 regulates integration of newly generated neurons in the adult brain. *Cell*. 130:1146–1158.

Eichenbaum H. 2017. Prefrontal-hippocampal interactions in episodic memory. *Nat Rev Neurosci*. 18:547–558.

Ennaceur A, Delacour J. 1988. A new one-trial test for neurobiological studies of memory in rats. 1: Behavioral data. *Behav Brain Res*. 31:47–59.

Hartung H, Cichon N, De Feo V, Riemann S, Schildt S, Lindemann C, Mulert C, Gogos JA, Hanganu-Opatz IL. 2016. From shortage to surge: a developmental switch in hippocampal-prefrontal coupling in a gene-environment model of neuropsychiatric disorders. *Cereb Cortex*. 26:4265–4281.

Heyser CJ, Ferris JS. 2013. Object exploration in the developing rat: methodological considerations. *Dev Psychobiol*. 55:373–381.

Ibi D, Nagai T, Koike H, Kitahara Y, Mizoguchi H, Niwa M, Jaaro-Peled H, Nitta A, Yoneda Y, Nabeshima T, et al. 2010. Combined effect of neonatal immune activation and mutant DISC1 on phenotypic changes in adulthood. *Behav Brain Res*. 206:32–37.

Janiesch PC, Kruger HS, Poschel B, Hanganu-Opatz IL. 2011. Cholinergic control in developing prefrontal-hippocampal networks. *J Neurosci*. 31:17955–17970.

Kakuda K, Niwa A, Honda R, Yamaguchi KI, Tomita H, Nojebuzzaman M, Hara A, Goto Y, Osawa M, Kuwata K. 2019. A DISC1 point mutation promotes oligomerization and impairs information processing in a mouse model of schizophrenia. *J Biochem*. 165:369–378.

Kamiya A, Kubo K, Tomoda T, Takaki M, Youn R, Ozeki Y, Sawamura N, Park U, Kudo C, Okawa M, et al. 2005. A schizophrenia-associated mutation of DISC1 perturbs cerebral cortex development. *Nat Cell Biol*. 7:1167–1178.

Koike H, Arguello PA, Kvajo M, Karayiorgou M, Gogos JA. 2006. Disc1 is mutated in the 129S6/SvEv strain and modulates working memory in mice. *PNAS*. 103:3693–3697.

Kruger HS, Brockmann MD, Salamon J, Ittrich H, Hanganu-Opatz IL. 2012. Neonatal hippocampal lesion alters the functional maturation of the prefrontal cortex and the early cognitive development in pre-juvenile rats. *Neurobiol Learn Mem*. 97:470–481.

Kvajo M, McKellar H, Arguello PA, Drew LJ, Moore H, MacDermott AB, Karayiorgou M, Gogos JA. 2008. A mutation in mouse Disc1 that models a schizophrenia risk allele leads to specific alterations in neuronal architecture and cognition. *PNAS*. 105:7076–7081.

Kvajo M, McKellar H, Drew LJ, Lepagnol-Bestel AM, Xiao L, Levy RJ, Blazeski R, Arguello PA, Lacefield CO, Mason CA, et al. 2011. Altered axonal targeting and short-term plasticity in the hippocampus of Disc1 mutant mice. *PNAS*. 108: 1349–1358.

Lipina TV, Zai C, Hlousek D, Roder JC, Wong AH. 2013. Maternal immune activation during gestation interacts with Disc1 point mutation to exacerbate schizophrenia-related behaviors in mice. *J Neurosci*. 33:7654–7666.

Meyer-Lindenberg A, Poline JB, Kohn PD, Holt JL, Egan MF, Weinberger DR, Berman KF. 2001. Evidence for abnormal cortical functional connectivity during working memory in schizophrenia. *Am J Psychiatry*. 158:1809–1817.

Meyer KD, Morris JA. 2008. Immunohistochemical analysis of Disc1 expression in the developing and adult hippocampus. *Gene Expr Patterns*. 8:494–501.

Meyer KD, Morris JA. 2009. Disc1 regulates granule cell migration in the developing hippocampus. *Hum Mol Genet*. 18:3286–3297.

Miyoshi K, Honda A, Baba K, Taniguchi M, Oono K, Fujita T, Kuroda S, Katayama T, Tohyama M. 2003. Disrupted-in-schizophrenia 1, a candidate gene for schizophrenia, participates in neurite outgrowth. *Mol Psychiatry*. 8:685–694.

Narayan S, Nakajima K, Sawa A. 2013. DISC1: a key lead in studying cortical development and associated brain disorders. *Neuroscientist*. 19:451–464.

Niwa M, Kamiya A, Murai R, Kubo K, Gruber AJ, Tomita K, Lu L, Tomisato S, Jaaro-Peled H, Seshadri S, et al. 2010. Knock-down of DISC1 by in utero gene transfer disturbs postnatal dopaminergic maturation in the frontal cortex and leads to adult behavioral deficits. *Neuron*. 65:480–489.

Nowack WJ, Janati A, Angtuaco T. 1989. Positive temporal sharp waves in neonatal EEG. *Clin Electroencephalogr*. 20:196–201.

Oberlander VC, Xu X, Chini M, Hanganu-Opatz IL. 2019. Developmental dysfunction of prefrontal-hippocampal networks in mouse models of mental illness. *Eur J Neurosci*. 50:3072–3084.

Ozeki Y, Tomoda T, Kleiderlein J, Kamiya A, Bord L, Fujii K, Okawa M, Yamada N, Hatten ME, Snyder SH, et al. 2003. Disrupted-in-Schizophrenia-1 (DISC-1): mutant truncation prevents binding to NudE-like (NUDEL) and inhibits neurite outgrowth. *PNAS*. 100:289–294.

Padilla-Coreano N, Bolkan SS, Pierce GM, Blackman DR, Hardin WD, Garcia-Garcia AL, Spellman TJ, Gordon JA. 2016. Direct ventral hippocampal-prefrontal input is required for anxiety-related neural activity and behavior. *Neuron*. 89:857–866.

Parent MA, Wang L, Su J, Netoff T, Yuan LL. 2010. Identification of the hippocampal input to medial prefrontal cortex in vitro. *Cereb Cortex*. 20:393–403.

Rasetti R, Mattay VS, White MG, Sambataro F, Podell JE, Zoltick B, Chen Q, Berman KF, Callicott JH, Weinberger DR. 2014. Altered hippocampal-parahippocampal function during stimulus encoding: a potential indicator of genetic liability for schizophrenia. *JAMA Psychiatry*. 71:236–247.

Ripke S, O'Dushlaine C, Chambert K, Moran JL, Kähler AK, Akterin S, Bergen SE, Collins AL, Crowley JJ, Fromer M, et al. 2013. Genome-wide association analysis identifies 13 new risk loci for schizophrenia. *Nat Genet*. 45:1150–1159.

Rossant C, Kadir SN, Goodman DFM, Schulman J, Hunter MLD, Saleem AB, Grosmark A, Belluscio M, Denfield GH, Ecker AS, et al. 2016. Spike sorting for large, dense electrode arrays. *Nat Neurosci*. 19:634–641.

Saito A, Taniguchi Y, Rannals MD, Merfeld EB, Ballinger MD, Koga M, Ohtani Y, Gurley DA, Sedlak TW, Cross A, et al. 2016. Early postnatal GABAA receptor modulation reverses deficits in neuronal maturation in a conditional neurodevelopmental mouse model of DISC1. *Mol Psychiatry*. 21:1449–1459.

Sauer JF, Struber M, Bartos M. 2015. Impaired fast-spiking interneuron function in a genetic mouse model of depression. *Elife*. 4:e04979.

Sawa A. 2019. DISC1 and its protein interactomes for mental function. *Biol Psychiatry*. 85:283–284.

Siapas AG, Lubenov EV, Wilson MA. 2005. Prefrontal phase locking to hippocampal theta oscillations. *Neuron*. 46:141–151.

Spellman T, Rigotti M, Ahmari SE, Fusi S, Gogos JA, Gordon JA. 2015. Hippocampal-prefrontal input supports spatial encoding in working memory. *Nature*. 522:309–314.

Stujenske JM, Spellman T, Gordon JA. 2015. Modeling the spatiotemporal dynamics of light and heat propagation for in vivo optogenetics. *Cell Rep*. 12:525–534.

Sullivan PF, Daly MJ, O'Donovan M. 2012. Genetic architectures of psychiatric disorders: the emerging picture and its implications. *Nat Rev Genet*. 13:537–551.

Szczurkowska J, Cwetsch AW, dal Maschio M, Ghezzi D, Ratto GM, Cancedda L. 2016. Targeted in vivo genetic manipulation of the mouse or rat brain by in utero electroporation with a triple-electrode probe. *Nat Protoc*. 11:399–412.

Tomita K, Kubo K, Ishii K, Nakajima K. 2011. Disrupted-in-Schizophrenia-1 (Disc1) is necessary for migration of the pyramidal neurons during mouse hippocampal development. *Hum Mol Genet*. 20:2834–2845.

Tomoda T, Hikida T, Sakurai T. 2017. Role of DISC1 in neuronal trafficking and its implication in neuropsychiatric manifestation and Neurotherapeutics. *Neurotherapeutics*. 14:623–629.

Tomoda T, Sumitomo A, Jaaro-Peled H, Sawa A. 2016. Utility and validity of DISC1 mouse models in biological psychiatry. *Neuroscience*. 321:99–107.

Trossbach SV, Bader V, Hecher L, Pum ME, Masoud ST, Prikulis I, Schäble S, de Souza Silva MA, Su P, Boulat B, et al. 2016. Misassembly of full-length disrupted-in-schizophrenia 1 protein is linked to altered dopamine homeostasis and behavioral deficits. *Mol Psychiatry*. 21:1561–1572.

Valeeva G, Nasretdinov A, Rychkova V, Khazipov R. 2019. Bilateral synchronization of hippocampal early sharp waves in neonatal rats. *Front Cell Neurosci*. 13:29.

Warburton EC, Brown MW. 2015. Neural circuitry for rat recognition memory. *Behav Brain Res*. 285:131–139.

Wolansky T, Clement EA, Peters SR, Palczak MA, Dickson CT. 2006. Hippocampal slow oscillation: a novel EEG state and its coordination with ongoing neocortical activity. *J Neurosci*. 26:6213–6229.

Xu X, Chini M, Bitzenhofer SH, Hanganu-Opatz IL. 2019. Transient knock-down of prefrontal DISC1 in immune-challenged mice causes abnormal long-range coupling and cognitive dysfunction throughout development. *J Neurosci*. 39:1222–1235.

Ye F, Kang E, Yu C, Qian X, Jacob F, Yu C, Mao M, Poon RYC, Kim J, Song H, et al. 2017. DISC1 regulates neurogenesis via modulating kinetochore attachment of Ndel1/Nde1 during mitosis. *Neuron*. 96:1041–1054e1045.